



**HAL**  
open science

## **Astrocytic centrin-2 expression in entorhinal cortex correlates with Alzheimer's disease severity**

Elisa Degl'Innocenti, Tino Emanuele Poloni, Valentina Medici, Francesco Olimpico, Francesco Finamore, Xhulja Profka, Karouna Bascarane, Castrese Morrone, Aldo Pastore, Carole Escartin, et al.

► **To cite this version:**

Elisa Degl'Innocenti, Tino Emanuele Poloni, Valentina Medici, Francesco Olimpico, Francesco Finamore, et al.. Astrocytic centrin-2 expression in entorhinal cortex correlates with Alzheimer's disease severity. *Glia*, 2024, 72 (12), pp.2158-2177. 10.1002/glia.24603 . hal-04780616

**HAL Id: hal-04780616**

**<https://hal.science/hal-04780616v1>**

Submitted on 13 Nov 2024

**HAL** is a multi-disciplinary open access archive for the deposit and dissemination of scientific research documents, whether they are published or not. The documents may come from teaching and research institutions in France or abroad, or from public or private research centers.













L'archive ouverte pluridisciplinaire **HAL**, est destinée au dépôt et à la diffusion de documents scientifiques de niveau recherche, publiés ou non, émanant des établissements d'enseignement et de recherche français ou étrangers, des laboratoires publics ou privés.



Distributed under a Creative Commons Attribution - NonCommercial 4.0 International License

## RESEARCH ARTICLE

# Astrocytic centrin-2 expression in entorhinal cortex correlates with Alzheimer's disease severity

Elisa Degl'Innocenti<sup>1,2</sup>  | Tino Emanuele Poloni<sup>3</sup>  | Valentina Medici<sup>3</sup>  |  
 Francesco Olimpico<sup>1</sup>  | Francesco Finamore<sup>1</sup>  | Xhulja Profka<sup>3</sup>  |  
 Karouna Bascarane<sup>4</sup>  | Castrese Morrone<sup>1</sup>  | Aldo Pastore<sup>1,5</sup>  |  
 Carole Escartin<sup>4</sup>  | Liam A. McDonnell<sup>1</sup>  | Maria Teresa Dell'Anno<sup>1</sup> 

<sup>1</sup>Fondazione Pisana per la Scienza ONLUS, San Giuliano Terme, Italy

<sup>2</sup>Department of Translational Research and New Technologies in Medicine and Surgery, University of Pisa, Pisa, Italy

<sup>3</sup>Department of Neurology and Neuropathology, Golgi-Cenci Foundation & ASP Golgi-Redaelli, Abbiategrasso, Italy

<sup>4</sup>Laboratoire des Maladies Neurodégénératives, Université Paris-Saclay, CEA, CNRS, MIRCen, Fontenay-aux-Roses, France

<sup>5</sup>Laboratorio NEST, Scuola Normale Superiore, Pisa, Italy

**Correspondence**

Maria Teresa Dell'Anno, Fondazione Pisana per la Scienza ONLUS, San Giuliano Terme, Italy.

Email: [mt.dellanno@fpscience.it](mailto:mt.dellanno@fpscience.it)

**Present addresses**

Valentina Medici, University of Piemonte-Orientale, Novara, Italy; and

Castrese Morrone, Telethon Institute of Genetics and Medicine (TIGEM), Pozzuoli, Italy.

**Funding information**

Fondazione Pisana per la Scienza, FPS grant

2018; ANR, Grant/Award Number:

#ANR21-CE17-0047-02; Fondo Beneficenza

Intesa San Paolo - Brain Bank Project

B-2022-0094

**Abstract**

Astrogliosis is a condition shared by acute and chronic neurological diseases and includes morphological, proteomic, and functional rearrangements of astroglia. In Alzheimer's disease (AD), reactive astrocytes frame amyloid deposits and exhibit structural changes associated with the overexpression of specific proteins, mostly belonging to intermediate filaments. At a functional level, amyloid beta triggers dysfunctional calcium signaling in astrocytes, which contributes to the maintenance of chronic neuroinflammation. Therefore, the identification of intracellular players that participate in astrocyte calcium signaling can help unveil the mechanisms underlying astrocyte reactivity and loss of function in AD. We have recently identified the calcium-binding protein centrin-2 (CETN2) as a novel astrocyte marker in the human brain and, in order to determine whether astrocytic CETN2 expression and distribution could be affected by neurodegenerative conditions, we examined its pattern in control and sporadic AD patients. By immunoblot, immunohistochemistry, and targeted-mass spectrometry, we report a positive correlation between entorhinal CETN2 immunoreactivity and neurocognitive impairment, along with the abundance of amyloid depositions and neurofibrillary tangles, thus highlighting a linear relationship between CETN2 expression and AD progression. CETN2-positive astrocytes were dispersed in the entorhinal cortex with a clustered pattern and colocalized with reactive glia markers STAT3, NFATc3, and YKL-40, indicating a human-specific role in AD-induced astrogliosis. Collectively, our data provide the first evidence that CETN2 is part of the astrocytic calcium toolkit undergoing rearrangements in AD and adds CETN2 to the list of proteins that could play a role in disease evolution.

**Abbreviations:** A $\beta$ , amyloid  $\beta$ ; AD, Alzheimer's disease; ALDH1L1, aldehyde dehydrogenase 1L1; CAA, cerebral amyloid angiopathy; <sup>11</sup>C DED, <sup>11</sup>C deuterium-L-deprenyl; CDR, clinical dementia rating; CETN2, centrin-2; CNS, central nervous system; CSF, cerebrospinal fluid; GABA,  $\gamma$ -amino butyric acid; GFAP, glial fibrillary acidic protein; JAK/STAT3, Janus kinase/signal transducer and activator of transcription 3; MAO-B, monoamine oxidase B; MCI, mild cognitive impairment; MMSE, mini mental state examination; NCD, neurocognitive disorders; NFAT, nuclear factor of activated T-cells; NFTs, neurofibrillary tangles; NOLD, normal old; NPs, neuritic plaques; PFA, paraformaldehyde; PRM, parallel reaction monitoring; pTAU, phospho Tau protein; PTM, post-translational modification; TDP-43, TAR DNA binding protein 43; Thio-S, thioflavin-S; XPC, xeroderma pigmentosum C complex.

Elisa Degl'Innocenti and Tino Emanuele Poloni equally contributed to the manuscript.

This is an open access article under the terms of the [Creative Commons Attribution-NonCommercial](https://creativecommons.org/licenses/by-nc/4.0/) License, which permits use, distribution and reproduction in any medium, provided the original work is properly cited and is not used for commercial purposes.

© 2024 The Author(s). GLIA published by Wiley Periodicals LLC.

## KEYWORDS

Alzheimer's disease, amyloid plaques, astrocytes, astrogliosis, centrin-2, entorhinal cortex

## 1 | INTRODUCTION

Alzheimer's disease (AD) is a form of dementia characterized by a progressive dysfunction of neuronal circuits, learning impairment, and memory loss (Querfurth & LaFerla, 2010). The extracellular depositions of amyloid beta (A $\beta$ ) peptides in amyloid plaques and the intracellular aggregation of hyperphosphorylated Tau protein (pTAU) in neurofibrillary tangles (NFTs) are two signature lesions of the disease, whose combined and multifocal presence in the cerebral cortex generates the neuritic plaques (NPs). AD clinical evolution reflects the spreading of lesions from the parahippocampal and hippocampal area to the parietal cortex and eventually to the whole neocortex, causing a progressive impairment of all cognitive domains. Therefore, the combined scores assigned to Amyloid depositions (Thal stages), pTAU (Braak stages), and NPs (CERAD—Consortium to Establish a Registry for AD) represent the ABC criteria to define AD diagnosis and pathological severity (i.e., no AD, low AD, intermediate AD, high AD) (Braak et al., 2006; Mirra et al., 1991; Montine et al., 2012; Thal et al., 2002).

Evidence has proven that the development of these lesions is accompanied by synaptic malfunction and neuronal loss (Perez-Nievas & Serrano-Pozo, 2018) thus supporting a “neurocentric view” of the disease. Currently, the AD drug development pipeline comprises 187 drugs whose main targets include amyloid protein, TAU protein, proteinopathies and proteostasis, lipids and lipoproteins, neurotransmitters, several different receptors, synaptic functions, inflammation, neuroprotection, oxidative stress, metabolism, blood flow, and microbiome in the gut-brain axis (Cummings et al., 2023). However, while current therapeutic approaches appear to temporarily improve some cognitive functions, they do not halt the progression of the disease.

In this framework, a major effort has been devoted to understanding the contribution of nonneuronal cells in AD pathogenesis. Astrocytes, in particular, have increasingly attracted attention, not only because of their contribution to many of the mechanisms and targets reported above (Khakh & Sofroniew, 2015) but also in consideration of genetic data showing that several genes, associated with the risk of developing AD (i.e., *SORL1*, *FERMT2*, *CLU*, and *APOE*) are mostly expressed in astrocytes (Arranz & De Strooper, 2019). Some studies suggest that astrocytes may actively contribute to the amyloidogenic process by expressing amyloid precursor protein and  $\beta$ -secretase (Frost & Li, 2017), while others promote their role in A $\beta$  clearance through the expression of A $\beta$ -degrading enzymes or by facilitating A $\beta$  transport through the perivascular drainage (Acosta et al., 2017).

Astrocytes in autaptic AD brain samples have been described as atrophic or reactive; two phenotypes that can be found in combination and may be indicative of the evolutionary stages in the neuropathological process. Atrophic astrocytes are suggestive of

dysfunctional cells that have lost their capacity to foster neuronal functioning, while at later stages, and in conjunction with signals from microglia, astrocytes are more frequently observed in a reactive state forming nests at the borders of amyloid plaques (Fakhoury, 2018; Verkhratsky et al., 2021). Reactive astrogliosis, canonically described as an increase in volume and thickening of astrocyte processes as well as by an overexpression of intermediate filament proteins (glial fibrillary acidic protein [GFAP], nestin, and vimentin) (Arranz & De Strooper, 2019; Chun & Lee, 2018; Escartin et al., 2021), has been described in close proximity to amyloid plaques (Garcia-Marin et al., 2007), condition that becomes progressively more extended with disease worsening. Astrogliosis has long been considered an epiphenomenon following neurodegeneration, nevertheless, recent investigations have shown that astrocytes appear to be engaged in a reactive state also before the onset of AD symptoms (Carter et al., 2012), thus suggesting that inflammatory changes precede clinical symptoms and highlighting the importance of immune states in AD pathogenesis (Chun & Lee, 2018).

On this basis, substantial effort has been devoted to the identification of pathways linked to the initiation and maintenance of the astroglia reactive state (Ben Haim, Carrillo-de Sauvage, et al., 2015). Among these, the Janus kinase/signal transducer and activator of transcription 3 (JAK/STAT3) pathway (Ben Haim, Ceyzeriat, et al., 2015; Ceyzeriat et al., 2018; Reichenbach et al., 2019) and the calcineurin/nuclear factor of activated T-cells c3 (NFATc3) pathway have been linked to astrocyte reactivity in AD (Abdul et al., 2009; Furman & Norris, 2014). Similarly, the astrocytic expression of chitinase-3 protein like-1 (also known as YKL-40) has been linked to AD-related neuroinflammation and predicts progression from normal cognition to mild cognitive impairment (MCI) that typically precedes dementia and frank neurodegeneration (Craig-Schapiro et al., 2010; Moreno-Rodriguez et al., 2020; Querol-Vilaseca et al., 2017; Zhang et al., 2018). Evidence has also shown that when astrocytes become reactive in AD, the monoaminoxidase-B/ $\gamma$ -aminobutyric acid (MAO-B/GABA) pathway is more activated, resulting in an increase in GABA release with consequent suppression of neuronal activity (Jo et al., 2014), as well as in the release of H<sub>2</sub>O<sub>2</sub>, which sustains the reactive state and fosters tauopathy, neuronal death, brain atrophy, and cognitive impairment (Chun et al., 2020).

Calcium is a well-known mediator of astrocytic intracellular signaling and in normal conditions exerts multifarious effects on synaptic functions, plasticity, and neural-network oscillations. In AD, astrocyte calcium dynamics and network responses become aberrant (Escartin et al., 2021), an observation that earned AD the definition of “chronic calciumopathy” (Querol-Vilaseca et al., 2016). Evidence from cultured astrocytes and organotypic slices shows that A $\beta$  exposure provokes spontaneous calcium oscillations and abnormal intracellular waves (Verkhratsky et al., 2017), while a chronic A $\beta$  insult may result in a pathological remodeling of the whole calcium signaling toolkit of



astrocytes, including several calcium-binding proteins and receptors (Querol-Vilaseca et al., 2016). We recently described the expression of the calcium-binding protein centrin-2 (CETN2) in human astrocytes and its distribution in the healthy human central nervous system (CNS) (Degl'Innocenti et al., 2022). With four EF-hand domains that enable calcium binding, CETN2 presents a chemical structure that resembles other known calcium sensors (i.e., troponin C or calmodulin) (Berridge et al., 2000), including the astrocytic marker S100B (Michetti et al., 2019). CETN2 labels astrocytes with a cytosolic pattern overlapping GFAP staining, with an overall distribution in the healthy brain that exhibits greater abundance in the isocortex (prefrontal and parietal cortices) compared with the allocortex (hippocampus and entorhinal cortex) where CETN2 expression is poorly detectable (Degl'Innocenti et al., 2022). Transcriptomics analyses of astrocytes microdissected from the brain samples of patients with different AD Braak stages have found changes in the expression of 32 genes associated with calcium signaling (Simpson et al., 2011; Verkhatsky, 2019) including calmodulins and calcium-calmodulin dependent kinases. Similarly, other components of the calcium signaling toolkit also exhibit variations with the disease, including calpain-10, NFAT, NF- $\kappa$ B, calcineurin, L-type calcium channels, or store-operated calcium channels (Verkhatsky, 2019). Nevertheless, whether CETN2 expression in astrocytes is altered in AD has not been explored so far.

To address this point, here we investigated the expression of CETN2 in a cohort of autopsy brain samples encompassing all AD phases, and all six Braak stages. Three cerebral areas were analyzed: the parahippocampal/entorhinal cortex, the prefrontal cortex, and the cerebellum. The parahippocampal/entorhinal area is severely affected from the beginning of the disease, first by tauopathy and later by A $\beta$  plaques and NP formation. The prefrontal cortex presents early A $\beta$  plaques but is affected by pTAU depositions only in the advanced stages, and finally, the cerebellum is typically involved by amyloid depositions only in severe AD and does not present pTAU aggregates.

The aim of the present investigation is to study the expression of CETN2 in these three anatomical areas along with the progression of the disease, assessed by means of clinical and neurohistological data, and determine whether CETN2 can be annotated as an indicator of reactive astrogliosis in humans.

## 2 | METHODS

### 2.1 | Subjects recruitment for histological analysis

The Abbiategrosso Brain Bank (ABB) at the Golgi Cenci Foundation (Milan, Italy) provided the autopsy human brain samples. Before death, all donors joined the donation program and underwent a systematic longitudinal multi-dimensional assessment to determine social, neuropsychological, biological, and clinical profiles, as previously described (Poloni et al., 2020). ABB donors included cognitively normal elderly individuals (NOLD) and patients affected by neurocognitive disorders (NCD) mainly due to AD. Joining the donation program is a personal decision, and complete awareness is needed. For

patients not deemed competent to sign the consent form, authorization from a legal guardian or next-of-kin was warranted, taking into account the wishes previously expressed by the subject. The ABB protocol is in accordance with the principles outlined by the Declaration of Helsinki (1964 and following amendments), and all ABB activities rigorously follow the ethical standards of the BrainNet Europe Code of Conduct (Klioueva et al., 2015; Klioueva et al., 2018). ABB procedures were performed under the supervision of the Italian Association of Alzheimer's patients and were approved by the Ethics Committee of the University of Pavia on October 6th, 2009 (Committee report 3/2009) (Guaita et al., 2013).

### 2.2 | Human brain dissection and characterization

The human brain samples were prepared as previously described (Poloni et al., 2020). Briefly, autopsies were conducted within a *post mortem* interval of 3–20 h, determined by an asystole of at least 20 min. After craniotomy, the brain, cerebellum, brainstem, and rostral cervical spinal cord were removed, separated, and then sectioned with a thickness of 1 cm. Tissue fixation was performed by leaving the slices in 10% buffered formalin solution for 5 days at 4°C and washed in a phosphate buffer for 2 days. Tissues were dehydrated through an automated processor (Histo-Line, ATP1000 Tissue Processor) and then soaked in xylene using metal or plastic molds. Sections were paraffin-embedded and subsequently cut into 8- $\mu$ m-thick slices using a rotary microtome (Leitz Laboratories 1400, ARM3600 HistoLine).

Luxol Fast blue staining for the visualization of gray and white matter was performed after the deparaffinization step incubating sections in a 0.1% luxol fast blue solution (Sigma-Aldrich #S3382) in ethanol 95% at 50°C. The following day, sections were cooled down at room temperature and quickly washed in ethanol 95% and mQ water prior to be immersed in a 0.05% lithium carbonate solution (Sigma-Aldrich #62470) for approximately 1 min. Sections were then differentiated in 70% ethanol until gray and white matter were visibly distinguishable. After a further washing in mQ water, samples were stained with a cresyl violet solution (Sigma-Aldrich #C5042) for at least 1 h at 40°C, rinsed with 95% ethanol and finally dehydrated with 100% ethanol and two immersions in xylene, 10 min each. Sections were coverslipped with mounting medium (Thermo Fisher Scientific #P36931).

According to the ABB immunohistochemistry protocol (Poloni et al., 2020), a complete neuropathological characterization was performed considering vascular as well as degenerative pathologies including A $\beta$  burden, p-Tau immunopositivity, synucleinopathies, and TAR DNA binding response protein-43 (TDP-43) inclusions. AD pathology severity was determined considering the Braak stage evaluation (Braak et al., 2006) and Thal's amyloid phases (Thal et al., 2002), according to Montine's scheme (low-intermediate-high AD pathology) (Montine et al., 2012). The impact of cerebrovascular pathology on cognition was graded using the Skrobot score (low-moderate-high) (Skrobot et al., 2016). Moreover, cerebral amyloid angiopathy (CAA) was graded through the 0–3 semiquantitative scale proposed by Love et al. (2014).



## 2.3 | Brain selection for the study

Sixteen brains were selected for this study. Cases with AD pathology, with or without concomitant vascular disease, were included (mild amounts of synucleinopathy and TDP-43 allowed). Cases affected by fronto-temporal dementia, Lewy bodies dementia (LBD), mixed AD/LBD pathology, and cases with other previous diseases that could have caused cognitive impairment were excluded. The *post mortem* interval did not exceed 20 h (range 3–20 h, mean 10 h). The 16 brains, comprising the entire spectrum of AD severity, were stratified according to the Braak stage: seven with Braak stage I–II (low AD), three with Braak stage III–IV (intermediate AD), and six with Braak stage V–VI (high AD). The selected cases included the following clinical diagnoses: three NOLD, four mild-NCD (namely, MCI), and nine major-NCD (namely, dementia), according to DSM-5 (Association AP, 2013). The clinical severity was graded through mini mental state examination (MMSE) and the clinical dementia rating (CDR) global score (Hughes et al., 1982), that assigns 0 to 5-point score based on the clinical severity (CDR 0: no dementia, CDR 0.5: MCI, CDR 1: mild dementia, CDR 2: moderate dementia, CDR 3: severe dementia, CDR 4: very severe dementia, and CDR 5: terminal dementia) (Dooneief et al., 1996; Heyman et al., 1987).

## 2.4 | Animals

Female triple transgenic (3xTg-AD) mice, which express human APP<sup>sw</sup> and human TauP301L under a Thy-1 promoter and have a point mutation in the mouse *Psen1* gene (PS1M146V), on a mixed C57BL/6J × 129Sv background were analyzed at 16 month-old (Oddo et al., 2003). Female C57BL/6J × 129Sv mice of the same age served as controls. Male APP/PS1dE9 transgenic mice possess a chimeric mouse/human *App* gene with the Swedish mutations K595N and M596L (APP<sup>sw</sup>) and the human *Psen1* variant lacking exon 9, all on a C57BL/6J background (Jankowsky et al., 2004). Both APP/PS1dE9 and nontransgenic littermates, used as controls, were sacrificed at 15 months-old. Twelve-month-old female APP<sup>NL-F/NL-F</sup> mice harbor the humanized A $\beta$  sequence under the endogenous APP mouse promoter with the Swedish (KM670/671NL) and the Beyreuther/Iberian mutations (I716F) (Saito et al., 2014). Nontransgenic littermates on the same C57BL/6J background served as controls. Efforts were made to minimize animal suffering, and care was supervised by veterinarians and animal technicians skilled in rodent healthcare and housing. The mice were housed under standard environmental conditions (12-h light–dark cycle, temperature: 22 ± 1°C, and humidity: 50%) with ad libitum access to food and water. 3xTg-AD mice were euthanized with an overdose of pentobarbital. One of their brain hemispheres was post-fixed in 4% paraformaldehyde (PFA) for 24 h. APP/PS1dE9 mice were euthanized with an overdose of pentobarbital and perfused with 4% PFA (8 mL/min). The APP<sup>NL-F/NL-F</sup> mice were anesthetized with a ip injection of ketamine (330 mg/kg) + medetomidine (1 mg/kg) followed by a subcutaneous injection of xylocaine (7 mg/kg). They were then cervically dislocated and perfused with PBS for 4 min at 8 mL/min and half their brain post-fixed for 24 h in 4% PFA. All mouse brains were cryoprotected and cut on a microtome into 30- $\mu$ m sections.

## 2.5 | Immunohistochemistry

Human brain specimens obtained from parahippocampal/entorhinal cortex, prefrontal cortex, and cerebellum were stewed at 58°C for 15 min and deparaffinized in xylene for 20 min. Rehydration was carried out by incubating brain sections, for 10 min at a time, in ethanol solutions at decreasing percentages (100%, 95%, 80%, and 70%), followed by a 10 min wash in PBS. Subsequently, sections were subjected to antigen retrieval at 121°C for 20 min in an automatic processor (2100 Retriever, BioVendor) using R-buffer A pH 6 (Electron Microscopy Science #62706-10). Samples were washed twice in mQ water and three times in PBS, before being incubated with blocking solution (5% horse serum and 0.3% Triton X-100 in PBS) for 1 h at room temperature in a humid chamber. Sections were then incubated with primary antibodies ON at 4°C. Primary antibodies were diluted in blocking solution as follows: anti-CETN2 (Merck Millipore #041624 and Biologend #698602, both diluted 1:500), anti-gial fibrillary acidic protein (GFAP; Dako #Z0334, 1:500), anti-Signal transducer and activator of transcription 3 (STAT3; Cell Signaling #8768, 1:500), anti-YKL40 (R&D System #AF2599, 1:50), anti-amyloid oligomers (Merck-Millipore #AB9234, 1:200), anti-pTau (Abcam #ab131354, 1:200), AT8 (Thermo Fisher Scientific #MN1020; 1:200), and anti-NFATc3 (Invitrogen #PA5-36101, 1:100).

The next day, sections were washed three times in PBS and incubated in blocking solution supplemented with Alexa Fluor secondary antibodies (Invitrogen #A11011, #A11004, #A32723, #A31571, Cell Signaling Technology #4416, all diluted 1:500) and DAPI (Sigma #32670, 1:500). The sections were finally treated with an auto-fluorescence eliminator (Merck-Millipore #2160) for 5 min and washed with 70% ethanol for 3 min before being coverslipped with mounting medium (Thermo Fisher Scientific #P36931). For thioflavin-S (thio-S) staining, immunolabeling was performed as previously described, with an additional incubation using a freshly prepared 0.01% thio-S solution in PBS for 20 min, performed after the last 3 min step in 70% ethanol. Excess of thio-S was removed with a PBS wash and the sections were then mounted, as described above.

Immunohistochemistry on mouse tissues was on performed 30- $\mu$ m-thick coronal or sagittal slices. Slices were rinsed in PBS and then subjected to antigen retrieval in a water bath with EDTA (pH 8) at 80°C for 20 min. After washing in PBS, the samples were blocked in 3% normal horse serum and 0.2% Triton X-100 in PBS for 1 h at room temperature. Slices were then incubated ON at 4°C with the following primary antibodies diluted in the blocking solution: anti-GFAP (Dako #Z0334, 1:500) and anti-CETN2 (Merck Millipore #041624, 1:500). After rinsing the slices three times in PBS, they were incubated with secondary Alexa Fluor-conjugated antibodies, as above mentioned, in 3% normal horse serum and 0.2% Triton X-100 in PBS for 1 h at room temperature. The slices were then rinsed three times with PBS before being mounted on SuperFrost® Plus (Thermo Fisher Scientific) slides and coverslipped with either Fluorsave™ (Calbiochem, Darmstadt, Germany) or Fluormount™ (Sigma) medium. Mouse images were acquired on a Leica TCS SP8 confocal microscope with 40 $\times$  and 63 $\times$  objectives.

## 2.6 | Quantitative image analysis

All images were acquired using an Olympus FluoView FV3000 confocal microscope with 30X silicone objective. The camera settings were adjusted at the start of the experiment and maintained for uniformity. The stereological quantification of CETN2<sup>+</sup> and GFAP<sup>+</sup> astrocytes was performed in blind, acquiring 16 images for each sample randomly distributed over the sample. Digital images were subsequently analyzed using the cell counter plugin of image processing software ImageJ, and CETN2<sup>+</sup> astrocyte quantification was expressed as a percentage of the total number of GFAP<sup>+</sup> astrocytes. For the quantification of the CETN2 immunoreactive area, 10 images were captured for each tissue section, each of which was processed by ImageJ software with the application of an intensity threshold level maintained throughout the whole image analysis. All quantitative comparisons were carried out on tissue sections that were stained at the same time and using the same antibody solutions, and whose images were analyzed using the same analysis settings. Plaque loading in the entorhinal cortex across diverse Braak stages was defined as the thio-S immunoreactive area, quantified with ImageJ software as described above. Thio-S<sup>+</sup> and CETN2<sup>+</sup> areas were expressed as percentages of the total area of the analyzed image.

Stereological analysis for reactive glia was performed by capturing 10 representative images for each section. Reactive glia was quantified using the cell counter plugin of the ImageJ software, and expressed as the percentage of STAT3<sup>+</sup>, NFATc3<sup>+</sup>, and YKL40<sup>+</sup> astrocytes out of the total CETN2<sup>+</sup> astrocytes.

## 2.7 | Western blot analysis

For the preparation of protein extracts, frozen brain samples were obtained from the parahippocampal/entorhinal cortex (three with Braak stage I and six with Braak stage V–VI). The tissue samples were dissected and homogenized in TBS buffer (20 mM Tris base, 137 mM NaCl, 2.7 mM KCl) supplemented with 1X Protease and Phosphatase Inhibitor Cocktail, EDTA-free (100X) (Thermo Fisher Scientific #78445). Sample homogenization was performed with a handheld homogenizer (Pro-Scientific Bio-gen PRO200). To minimize sample heating, the tissue was homogenized using four “8s homogenization plus 30s rest” cycles while being kept on ice. Lysates were cleared by centrifugation at 20,000 × *g* for 30 min. Supernatants were recovered and quantified using the Bradford method (Merck-Millipore #B6916) using a microplate reader (Tecan infinite F200). Samples (120 μg) were mixed with 4x Laemmli protein sample buffer (Bio-Rad #1610747) containing 10% β-mercaptoethanol (Sigma-Aldrich # M6250) and heated for 5 min at 95°C. Samples were loaded on SDS-PAGE 4%–20% Mini-PROTEAN<sup>®</sup> TGX<sup>™</sup> Precast Protein Gels (Bio-Rad #4561094) using the mini-cell system. Tris/Glycine/SDS running buffer (Bio-Rad #1610732) was used for electrophoresis. Following electrophoresis, proteins were transferred onto 0.2 μm nitrocellulose membranes (Bio-Rad #1704158) using a wet-blot (Bio-Rad) transfer system. After exposing the proteins to the blocking solution containing 5% milk in PBS-Triton 0.1% for 1 h

at room temperature, membranes were incubated ON with primary antibodies at 4°C anti-CETN2 (Merck Millipore #041624, 1:1000) and anti-β-ACTIN (Cell Signaling #4967, 1:1000), all diluted in blocking solution. After primary antibody incubation, horseradish peroxidase (HRP) conjugated secondary antibodies (anti-rabbit IgG-HRP Santa Cruz # sc-2357, 1:2000 and anti-mouse m-IgGκ BP-HRP Santa Cruz # sc-516102, 1:2000) were applied for 1 h at room temperature. Membranes were then washed three times with PBS Triton 0.1% and visualized using SuperSignal<sup>™</sup> West Femto Maximum Sensitivity Substrate (Thermo Fisher Scientific #34094). Blots images were then acquired with an enhanced chemiluminescence detection system Chemidoc (Bio-Rad).

## 2.8 | Expression and purification of human CETN2

Human CETN2 was retrieved from HEK293 cells (Sinobiological #14983-H08H) or it was purified from transformed *E. Coli* according to the following protocol. Briefly, an ON culture of *E. Coli* strain BL21 (DE3; Thermo Fisher #ECO114) transformed with a pET-28a construct (Twin Helix) was diluted in distilled water at a 1:100 ratio and induced at an  $A_{600}$  of 0.5–0.6 for 4 h by adding 0.8 mM β-D-1-thiogalactopyranoside (IPTG). All cultures were performed in Luria Bertani (LB) media with 50 μg/mL kanamycin at 37°C. Cells were resuspended 1:5 (w/v) in buffer A (20 mM Tris-HCl pH 7.4, 100 mM NaCl, 20 mM Imidazole) and lysed by freeze-thawing cycles while being kept refrigerated. The bacterial lysate was then centrifuged for 30 min at 14,000 × *g* at 4°C, and the clear supernatant was recovered. The supernatant containing proteins was loaded onto a HisTrap-FF 1 mL column (Cytiva #17531901) and eluted with a 150–500 mM Imidazole gradient in buffer B (20 mM Tris HCl pH 7.4, 100 mM NaCl, 500 mM Imidazole). Fractions containing the expected protein band were pooled and loaded onto PD-10 desalting column (Cytiva #17-0851-01), and eluted with buffer C (20 mM TrisHCl pH 7.4, 100 mM NaCl). The solution containing the protein was then concentrated with an Amicon Ultracel 10K (Merck-Millipore # UFC501024), and stored at –20°C. SDS-PAGE was used to assess the purity of the proteins, and their concentration was determined with a Sigma protein assay kit (Bradford reagent, Merck-Millipore #B6916-500ML).

## 2.9 | In-gel protein digestion and targeted mass spectrometry

Protein extracts from brain samples of three Braak stage I and six Braak stage V–VI patients were run on a polyacrylamide gel (4%–20% Mini-PROTEAN<sup>®</sup> TGX<sup>™</sup> Precast Protein Gels, Bio-Rad #4561094) followed by Coomassie blue staining. The bands at 20 and 25 kDa were excised from each sample lane and washed with 50 mM ammonium bicarbonate/50% acetonitrile to remove the Coomassie dye. The gel slices were dehydrated with acetonitrile and then incubated with 10 mM dithiothreitol at 56°C followed by 55 mM iodoacetamide at room temperature. Gel slices were dehydrated and incubated with 12.5 ng/μL trypsin/lys-C endoproteases (Promega, Trypsin/Lys-C

Mix, Mass spec Grade) for 18 h at 37°C. Peptide extraction from gel slices was performed using 50% acetonitrile/5% formic acid (FA) and then lyophilized. The dried peptides were then resuspended in 0.1% FA and desalted with C<sub>18</sub> spin columns (Pierce™ Peptide Desalting Spin Column). The eluted peptides were evaporated to dryness and resuspended in 10% FA for subsequent Liquid Chromatography Tandem Mass Spectrometry (LC-MS/MS) analysis using an Easy-nLC1000 (Thermo Scientific) coupled to an Orbitrap Fusion (Thermo Scientific). The liquid chromatography set-up consisted of an Acclaim PepMap™ 100 trap column (C<sub>18</sub>, 3 μm, 100 Å, 75 μm × 2 cm; Thermo Scientific) and a PepMap™ RSLC analytical column (C<sub>18</sub>, 2 μm, 100 Å, 75 μm × 50 cm; Thermo Scientific). Peptides were separated using a segmented gradient of 5%–23% solvent B in 52 min, up to 33% B in 7 min, and up to 60% B in 13 min at a flow rate of 300 nL/min (solvent A: 0.1% FA in water; solvent B: 0.1% FA in acetonitrile). The LC output was coupled to an EASY nano-spray source operating at 2.1 kV in positive-ion mode and directly interfaced with the Orbitrap Fusion mass spectrometer. The mass spectrometer was operated in parallel reaction monitoring (PRM) mode for the detection of CETN2. A list of 28 transitions (precursor/fragments pairs) corresponding to 27 CETN2 peptides were previously defined via data-dependent acquisition (DDA) analysis of a CETN2 protein standard. For the DDA method, peptide ions were recorded in a MS1 survey scan at a resolving power of 120,000 with a scan range 350–1650 m/z, a maximum injection target of 50 ms and an AGC target of  $4 \times 10^5$ ; precursor ions were selected within an isolation window of 1.4 m/z, an AGC target of  $2 \times 10^4$ , with a maximum injection time of 50 ms and fragmented using high-collisional energy activation (HCD) at 24% NCE (normalized collision energy). Fragment ion spectra were detected in a dual pressure linear ion trap with a dynamic exclusion of 20 s and a total cycle time of 3 s. The PRM method cycled across the 28 transitions for the entire peptide elution time, using a resolving power of 15,000 with an isolation width of 1.6 m/z, an ACG target of  $10^4$ , a maximum injection time of 22 ms, and the same 24% NCE HCD activation. The entire cycle time to acquire all the transition was ~1.7 s, thus allowing the collection of ~12 points per chromatographic peak. Raw data were analyzed using Skyline v21.2 software. The peak areas of fragment ions were extracted, using a mass error <10 ppm, and the most intense fragment ions were normalized over the entire total ion current (TIC) from the MS2 scan of each run. Peptide abundances were calculated by summing fragment ion intensities across the peptide elution profile.

## 2.10 | Peptide mass fingerprint analysis

Gel bands that had been stained with Coomassie blue were cut out, de-stained, reduced with dithiothreitol (Merck Life Science), alkylated with iodoacetamide, and digested using trypsin (Promega). The resulting peptides were then analyzed using an Ultimate 3000 RSLC nano coupled to a Q-Exactive HF-X Orbitrap mass spectrometer (Thermo Fisher Scientific) equipped with an Easy Spray ESI ion source. Peptides were separated using gradient elution at a flow rate of 300 nL/min at

35°C using a PepMap™ RSLC C18 column, 75 μm × 150 mm, 2 μm, 100 Å (Thermo Fisher Scientific). The LC gradient started at 5% phase B and increased to 36% B in 60 min (phase A: 0.1% FA in water; phase B: 0.1% FA in acetonitrile).

The MS/MS spectra were obtained in “data-dependent scan” mode. MS1 survey scans were performed at a resolving power of 120 k with a scan range 350–1650 m/z, a maximum injection time of 100 ms and an AGC target of  $3 \times 10^6$ ; precursor ions were selected within an isolation window of 1.4 m/z, an AGC target of  $2 \times 10^4$ , a maximum injection time of 50 ms and fragmented using HCD at 27% NCE. Fragment ion spectra were detected in the orbitrap at a resolving power of 30 k with a scan range 350–1650 m/z. MS/MS was performed with a dynamic exclusion of 20 s and a total cycle time of 3 s. The LC-MS/MS data were analyzed using BioPharma Finder software (v. 2.0, Thermo Fisher Scientific) with the CETN2 sequence as input protein sequence. To identify post-translational modifications, the data analysis was sequentially repeated with acetylation, glycation, phosphorylation, ubiquitination, methionine oxidation, and carbamylation as variable modifications. Only peptides identified with MS/MS confidence scores greater than 90% and mass tolerance within ±1.5 ppm were considered.

## 2.11 | Statistical analysis

Statistical power analysis to ascertain the suitability of the sample size was conducted with the Sample Size Calculator software (<https://homepage.univie.ac.at/robin.ristl/samplesize.php>) using one-way ANOVA test with Bonferroni correction. Normality of all datasets was evaluated with the Shapiro–Wilk test. The stereological quantification of CETN2+ and GFAP+ astrocytes, and the immunoreactive area in the entorhinal, prefrontal cortices and cerebellum were analyzed with Kruskal–Wallis test corrected using Dunn's multiple comparisons test. Targeted mass spectrometry CETN2 quantification between Braak stage I versus Braak stage V–VI samples was performed using a *t*-test. The correlation between CETN2+ area and thio-S+ and pTau+ areas were quantified with the Pearson correlation test. The correlation between CETN2+ astrocytes and MMSE and CDR scores were quantified by means of Spearman correlation test. CETN2 quantification in the entorhinal cortex was performed using an unpaired *t*-test with Welch's correction. Data were analyzed with GraphPad Prism 6.0 and XLSTAT for Microsoft Excel.

## 3 | RESULTS

### 3.1 | Demographic, cognitive, and neuropathological characteristics of the cohort

#### 3.1.1 | Clinical data

Demographic and clinical features of the study participants are shown in Table 1. All subjects, except 10 and 13, had various combinations of comorbidities including hypertension, diabetes, cancer, and



**TABLE 1** Demographic, cognitive, and neuropathological characteristics of the cohort.

Samples	Gender	Comorbidity	ApoE	NCD clinical diagnosis	MMSE	CDR	Age at death	Death cause	Thal phase	Braak stage	AD scoring (Montine)	CAA (Love)	Additive pathologies	Vascular pathology (Skrobot)
1	M	CVD; DM2	3//3	NOLD	26	0	79	TCD	1	I	Low	No	No	Low
2	F	CBVD	3//3	Mild-NCD (MCI)	27	0.5	79	Sepsis	3	I	Low	No	alpha-syn	Low
3	F	CVD; CBVD	3//3	Mild-NCD (MCI)	29	0.5	81	Cachexia	3	I	Low	1P; 1M	No	Moderate
4	F	AHT	3//4	Mild-NCD (MCI)	27	0.5	79	TCD	4	II	Low	2M	No	Low
5	F	AHT	3//4	NOLD	29	0	80	TCD	3	II	Low	3Pcap; 3M	No	Low
6	F	AHT; CVD; CBVD	3//3	Mild-NCD (MCI)	24	0.5	84	Heart failure	4	II	Low	2Pcap; 2M	No	Moderate
7	F	CVD	2//3	NOLD	29	0	79	Heart failure	1	II	Low	1P; 2M	alpha-syn	Low
8	F	CVD; CBVD; DM2	4//4	Major-NCD (AD; VaD)	0	5	79	Hemorrhage	3	III	Int	3Pcap; 3M	No	High
9	F	AHT; CBVD; DM2	3//4	Major-NCD (AD)	21	2	82	Cachexia	4	III	Int	2M	No	Moderate
10	F	No	3//4	Major-NCD (AD)	10	3	80	Arrhythmia	5	IV	Int	3Pcap; 3M	TDP-43	Low
11	F	CVD; CBVD	3//3	Major-NCD (AD)	2	4	85	Arrhythmia	5	V	high	2Pcap; 3M	TDP-43	Moderate
12	F	CVD; DM2	2//3	Major-NCD (AD)	0	5	78	Arrhythmia	4	IV-V	High	No	No	Low
13	M	004Eo	3//3	Major-NCD (AD)	4	4	80	Arrhythmia	5	VI	High	2M	TDP-43	No
14	F	AHT; CBVD	3//4	Major-NCD (AD)	0	5	89	Cachexia	5	V	High	3Pcap; 3M	TDP-43	Moderate
15	M	AHT	3//4	Major-NCD (AD)	5	4	75	Cachexia	5	V-VI	High	2P; 2M	alpha-syn	Low
16	F	AHT	3//4	Major-NCD (AD)	0	5	95	Cachexia	5	VI	High	1P; 2M	TDP-43	Low

Abbreviations: AD, Alzheimer's disease; AHT, arterial hypertension; alpha-syn, alpha-synuclein; CAA, cerebral amyloid angiopathy; 1 mild; 2 moderate; 3 severe; cap, capillary involvement; CBVD, cerebrovascular disease; CDR, clinical dementia rating scale; CVD, cardiovascular disease; DM2, diabetes mellitus type 2; F, female; M, male; M, meningial; MCI, mild cognitive impairment; NCD, neurocognitive disorder; NOLD, normal old; P, parenchymal; TCD, terminal cancer disease; TDP-43, TAR DNA-binding protein 43; VaD, vascular dementia.

cerebrovascular or cardiovascular diseases. Eight cases were heterozygous for the ApoE 4 allele, the best-known genetic risk factor for late onset dementia. Three subjects were cognitively normal (NOLD), whereas 13 presented a history of NCD (4 of them had MCI and 9 had dementia). During life, all were cognitively assessed with the MMSE test, performed within 6 months before death. Cognitively normal cases and those with MCI had a mean MMSE score of 27.3 (range 24–29); subjects with dementia had a MMSE score of 21 or less (range 0–21). At death, the mean age was 82 years old (range: 75–95). The three NOLD subjects had a CDR score of 0, and all 4 MCI subjects had a CDR score of 0.5. Out of the nine patients with dementia, one showed moderate dementia (CDR score 2), four showed severe to very severe dementia (CDR score 3–4), and three showed terminal dementia (CDR score 5). Death causes included sudden arrhythmia, heart failure, hemorrhage, sepsis, and cachexia due to terminal dementia or cancer. The mean *post mortem* interval was 10.2 h.

### 3.1.2 | Neuropathological assessment

The neuropathological assessment of the 16 cases is summarized in Table 1. The analyzed brains comprised the entire AD spectrum, including seven cases with Braak stage I–II, and Thal phases between 1 and 4 (low AD); three cases with Braak stage III–IV, and Thal phases between 3 and 5 (intermediate AD); and six cases with Braak stage V–VI, and Thal phases between 4 and 5 (high AD). Representative images of pTAU (AT8) immunostaining for Braak staging are included in Supporting Information (Figure S1a–d). Five of the seven cases with a Braak I–II stage (low AD) presented a fairly extensive presence of amyloid up to involving the basal ganglia, and also slightly affecting the rostral part of the brainstem in two cases. Ten cases had meningeal and parenchymal cerebral amyloid angiopathy (CAA), mainly parieto-occipital, of which six also showed capillary involvement (cap CAA), while three cases had only meningeal CAA. Eight subjects presented mild additive proteinopathies. In particular, three of them had incidental Lewy type synucleinopathy, according to the definition by Beach et al. (2009), whereas five had mild limbic TDP-43 deposits. With regard to TDP-43 aggregates, these are neuropathological pictures of LATE (Limbic-predominant Age-related TDP-43 Encephalopathy) with limited TDP-43 deposits in the amygdala and/or hippocampus, which are often observed in elderly patients with AD (LATE stages 1–2), according to Nelson's scheme (Nelson et al., 2019). The vascular burden was low in nine cases, moderate in five cases, and high in one case. One subject presented no vascular pathology.

## 3.2 | CETN2 immunoreactive astrocytes increase with AD progression in entorhinal cortex

In order to elucidate whether CETN2 expression in astrocytes is affected by AD progression, we performed an immunohistochemical and biochemical assessment in three diverse anatomical areas. We investigated CETN2 expression in the entorhinal and prefrontal

cortices, affected by the disease in different timeframes, and in the cerebellum, typically less affected (Hempel et al., 2021). In the entorhinal cortex, we observed that patients classified as Braak stage I and II showed regularly shaped GFAP-positive (GFAP+) astrocytes, with few exhibiting CETN2 co-expression. Specifically, we estimated  $24.8\% \pm 2.6\%$  CETN2+/GFAP+ astrocytes for Braak stage I, and  $27.5\% \pm 3.0\%$  for Braak stage II (Figure 1a–a2,b–b2,e). Progression toward advanced disease stages led to the phenotypic change in astrocytes indicative of astrogliosis, such as the increased immunoreactivity for GFAP, without alteration in the number of astrocytes (Figure S1e,f) (Ben Haim, Carrillo-de Sauvage, et al., 2015; Serrano-Pozo, Gomez-Isla, et al., 2013). On the other hand, the number of CETN2+ astrocytes increased following disease progression:  $33.3\% \pm 11.5\%$  CETN2+/GFAP+ astrocytes were estimated for Braak stage III–IV and raised to  $76.6\% \pm 3.4\%$  for Braak stage V–VI (Figure 1c–c2,d–d2,e). CETN2+ astrocyte increment reached statistical significance for Braak stage V–VI in comparison with stage I (Figure 1e, adj *p* value = .01) and stage II (adj *p* value = .04), supported also by an increase in CETN2 immunoreactive area (Figure 1f, Braak I versus Braak V–VI adj *p* value = .04 and Braak II versus Braak V–VI adj *p* value = .03). No correlation was observed with respect to the age of patients (Figure S1g, Pearson correlation analysis *p* = .25, *r* = .30, *R*<sup>2</sup> = .09).

The abundance of CETN2 in the entorhinal cortex was also quantified through biochemical assessment. Western blot analysis of Braak I versus Braak V–VI lysates allowed the detection of the CETN2 band at the expected molecular weight of 20 kDa (Figure 1g and Figure S2a). The band appeared faint in Braak I samples, while a significantly stronger signal was observed in Braak V–VI samples (Figure 1g,h; Welch's *t*-test *p* = .03). Of note, the CETN2 immunoblot revealed an additional band at ~25 kDa for both Braak stages (Figure 1g and Figure S2a). To exclude a nonspecific binding of the anti-CETN2 antibody, human recombinant CETN2 (rCETN2) purified from HEK293 cells was revealed by means of Coomassie and silver stainings (Figure S2b). Both procedures allowed the detection of a major 20 kDa band and of an additional ~25 kDa band (Figure S2b), and both were also revealed by two different anti-CETN2 antibodies (clone W16110A and clone 20H5) (Figure S2c). rCETN2 was also produced in *E. Coli*. Interestingly, while clone 20H5 resolved human rCETN2 in two bands and in a concentration-dependent manner, rCETN2 from *E. Coli* was resolved in one single band at the expected molecular weight of 20 kDa (Figure S2d). To ascertain the nature of the upper band, we utilized mass spectrometry applied on human rCETN2 upon excision of both bands from the polyacrylamide gel (Figure S2e). The analysis revealed the presence of post-translational modifications (PTMs) uniquely detectable in the 25 kDa CETN2 band (modified CETN2–mCETN2), namely acetylation of lysine 30 and carbamylation of lysine 22 and 103 (Figure S2f; Table S1).

To confirm the data from the stereological and biochemical assays, an antibody independent method was also applied. Targeted-mass spectrometry was used to quantify CETN2 in the entorhinal cortices of the two most informative Braak stages. Proteins extracted from Braak I and Braak V–VI entorhinal cortices were subjected to SDS-PAGE, then the 20 and 25 kDa bands detected by Coomassie



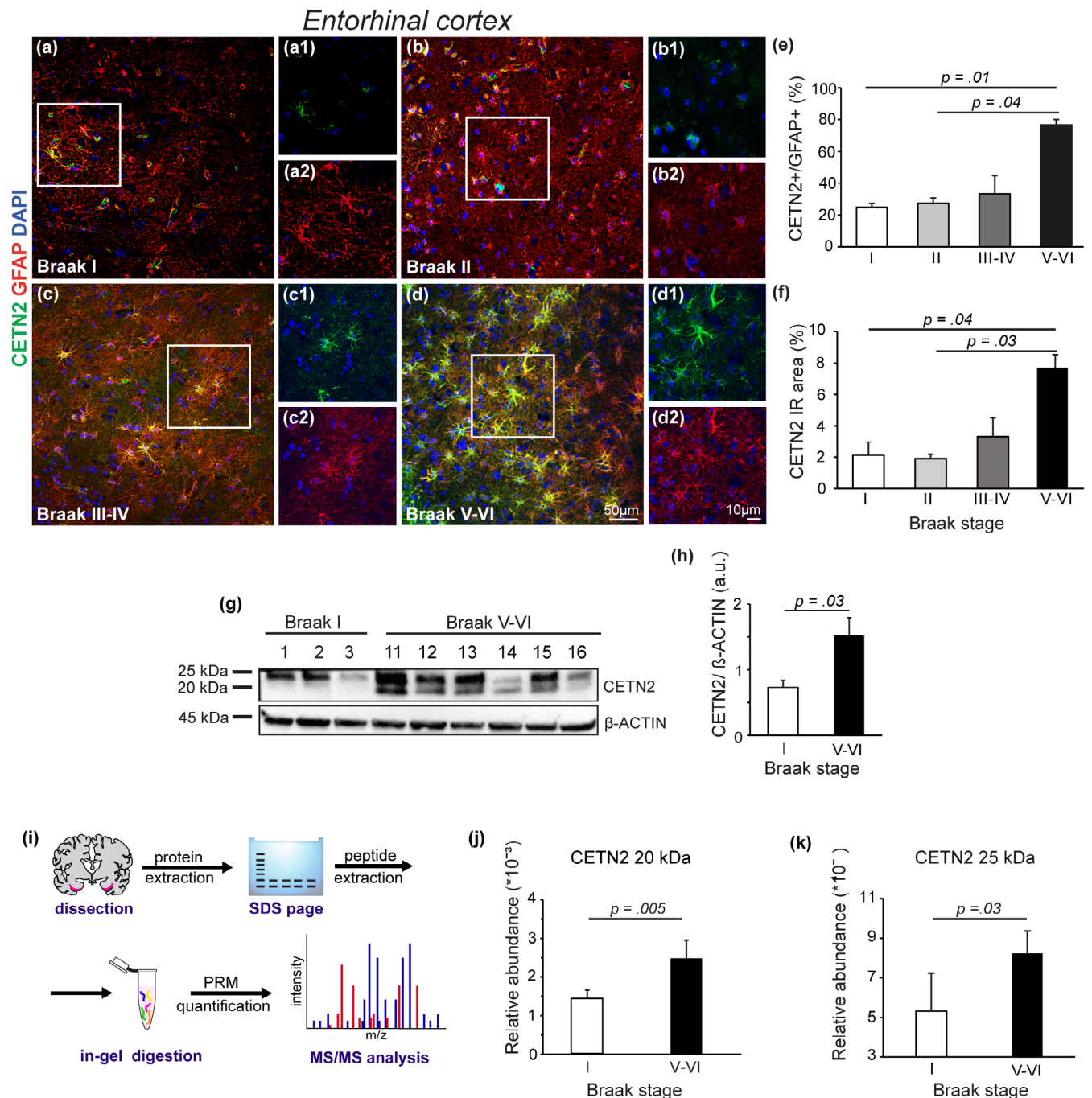


**FIGURE 1** Entorhinal cortex CETN2+ astrocytes significantly increase with disease severity. (a–d2) Immunostaining of human entorhinal cortices at Braak stages: I (a–a2), II (b–b2), III–IV (c–c2), and V–VI (d–d2) showing CETN2+ (green) and GFAP+ (red) astrocytes. Representative images show an increase of CETN2 immunopositivity in astrocytes along with disease progression. Insets (a1–d2) show magnifications of (a–d). (e) Histogram representing the percentage of CETN2+ astrocytes over the total of GFAP+ astrocytes through Braak stages I–VI. The comparison between Braak stage I versus V–VI, and Braak II versus V–VI, shows a statistically significant difference (Kruskal–Wallis test corrected for Dunn's test; adj  $p$  value = .01, adj  $p$  value = .04, respectively). (f) Histogram illustrating the percentage of CETN2 immunoreactive area in all Braak stages (Kruskal–Wallis test corrected for Dunn's test, Braak I versus Braak V–VI adj  $p$  = .04 and Braak II versus Braak V–VI adj  $p$  value = .03). (g) Immunoblot analysis on entorhinal cortex samples from Braak I and Braak V–VI staged brains blotted for CETN2 and  $\beta$ -Actin. (h) Histogram representing the CETN2 signal normalized on  $\beta$ -Actin for Braak stages I and V–VI. Welch's  $t$ -test shows statistically significant difference between the two groups (unpaired  $t$ -test with Welch's correction,  $p$  = .03). Histograms show mean  $\pm$  SEM. (i) Workflow of the procedural steps of targeted mass spectrometry performed on protein extracts from entorhinal cortices. (j) CETN2 20 kDa band abundance in Braak stage I and Braak stage V–VI patients. Histogram represents mean  $\pm$  SD. ( $t$ -test,  $p$  = .005). (k) CETN2 25 kDa band abundance between Braak I and Braak V–VI staged patients. Data show mean  $\pm$  SD ( $t$ -test,  $p$  = .03). Scale bars: (a–d): 50  $\mu$ m; (a1–d2): 10  $\mu$ m. PRM, parallel reaction monitoring.



staining were isolated, and processed for in-gel proteolytic digestion (Figure 1i). The resulting proteolytic peptides were analyzed by PRM, which allowed the identification of CETN2-specific peptides from the 20 and 25 kDa bands (Table S1). The relative abundance of the CETN2 peptides from 20 and 25 kDa bands was used to quantify CETN2 for Braak stage I and Braak stage V–VI patients. The comparison highlighted a significant difference between the two groups for both the CETN2 20 and 25 kDa bands (Figure 1j *t*-test,  $p = .005$ ; Figure 1k *t*-test,  $p = .03$ ). Peptides and protein intensities obtained from each patient are available in Table S1. CETN2 expression was also investigated across all Braak stages in the prefrontal cortex and cerebellum, but no significant changes were detected (Figure 2). Furthermore, CETN2 immunostaining was performed on the hippocampal areas and entorhinal cortices of three different AD mouse models: 3xTg-AD, APP/PS1dE9, and APP<sup>NL-F/NL-F</sup>. No CETN2+ astrocytes were observed in the hippocampus and the entorhinal cortex of these models nor in WT mice, as previously reported (Degl'Innocenti et al., 2022) (Figure S3a–d,f–i,k–n). However, CETN2 expression was physiologically observed in the ependymal cells (Figure S3e,j,o). Overall, the results obtained from three distinct technical approaches confirmed a significant increase in CETN2 astrocytic expression specific to AD in humans. This increase correlates with Braak staging, becoming particularly significant in the most severely affected entorhinal cortices.

### 3.3 | CETN2 immunoreactivity correlates with cognitive decline and pathological burden

Next, we sought to determine whether the degree of CETN2 correlation to AD progression was also extendable to clinical data. A correlation analysis between the average percentage of CETN2+ astrocytes for each patient and the MMSE (Figure 3a) and CDR scores (Figure 3b) was performed. Both analyses indicated that the percentage of CETN2+ astrocytes is strongly associated with worsening cognitive impairment. CETN2+ astrocytes increased with the lowering of the MMSE scores and with the increasing of the CDR scores, reaching an average of  $76.6\% \pm 3.4\%$  CETN2+ astrocytes for cases with MMSE scores of 0–5 and a CDR score of 4–5, corresponding to Braak stage V–VI.

Together with the temporo-basal isocortex, the entorhinal cortex is known for being primarily affected by AD pathology (Thal et al., 2000). Since A $\beta$  plaques and NFTs are thought to trigger astrocyte and microglial reactions (Serrano-Pozo et al., 2011; Serrano-Pozo, Gomez-Isla, et al., 2013; Serrano-Pozo, Muzikansky, et al., 2013), we next investigated the association of CETN2 astrocytic expression with pTAU-positive NFTs and thio-S immunoreactive A $\beta$  plaques in the entorhinal cortices. Immunopositivity for pTAU showed consistency with Braak staging and reflected the progressive deposition of NFTs in diseased tissues. CETN2 immunoreactivity tracked the abundance of pTAU: CETN2 displayed a poor signal in Braak stage I (Figure 3c–d1) and then a progressive increase in Braak II and III–IV (Figure 3e–h1), reaching the highest signal in Braak stage V–VI (Figure 3i–j1), along

with the presence of pTAU immunoreactive NPs. The deposition of NPs, more prominent in Braak V–VI-staged brains, was indeed accompanied by a higher number of CETN2+ astrocytes, which mostly appeared oriented in a shell-like configuration around the lesions (Figure 3i–j1). Accordingly, the correlation analysis in all samples of our cohort demonstrated a significant degree of association between the pTAU+ area and the CETN2+ area (Figure 3k; Pearson correlation coefficient  $r = .65$ ;  $R^2 = .43$ ;  $p = .006$ ).

Similarly, CETN2 labeling was associated with thio-S staining, used for the detection of fibrillar amyloid plaques (Figure 3l–s1). In subjects classified as Braak stage I, CETN2 immunoreactivity was scarcely appreciable (Figure 3l–m1). On the other hand, AD progression toward more severe stages, with an increasing amyloid load and NP formation, was accompanied by a proportional increment in CETN2 expression in astrocytes (Figure 3n–s1). Accordingly, the quantification of the overall CETN2+ area across all Braak stages resulted in a significant correlation with the amount of fibrillary amyloid and NPs (Figure 3t; Pearson's correlation coefficient  $r = .97$ ;  $R^2 = .94$ ;  $p < .0001$ ).

A more detailed study was then conducted on entorhinal cortex samples from severe AD patients (Braak stage V–VI), utilizing anti-A $\beta$  oligomer (A $\beta$ o) staining. Here, CETN2+ astrocytes were clearly detectable in the gray matter of the entorhinal cortex and, to a lesser extent, in the white matter, distinguished by means of luxol fast blue staining (Figure 4a). Unlike GFAP, which exhibited a more uniform distribution across layers (Figure 4b), the CETN2 pattern appeared clustered, thus indicating that only a fraction of GFAP+ cells co-expressed CETN2 (Figure 4c). In particular, CETN2 immunoreactivity was detectable in the molecular layer and, in a more prominent way, in pyramidal and granular cortical layers of the allo-mesocortex in correspondence of a larger amyloid burden (Figure 4c).

Not all CETN2 immunoreactive astrocytes were located close to plaques (Figure 4d–f), but for those that closely surrounded A $\beta$  deposits, we asked whether they exhibited any selectivity. We investigated three types of amyloid aggregates, namely coarse-grained (Figure 4g) and classic cored plaques (Figure 4h), distinguishable by their morphology, and vascular deposits referred to as CAA type 1 (Figure 4i) (Boon et al., 2020). However, CETN2+ astrocytes did not show a peculiar tropism and were ubiquitously observed surrounding all types of amyloid plaques.

### 3.4 | CETN2 labels reactive astrocytes in diseased entorhinal cortex

Given the large abundance of CETN2+ astrocytes in correspondence with amyloid deposits, we next asked whether CETN2+ astrocytes also exhibited other known features of reactive astrogliosis. Recent evidence has shown that many parameters need to be considered to fulfill the definition of reactive glia beyond the simple morphometric assessment and enhanced GFAP immunoreactivity (Escartin et al., 2021). We explored the co-expression of CETN2 with other annotated reactive glia markers, namely STAT3, downstream effector of the JAK/STAT3 pathway (Ben Haim, Ceyzeriat, et al., 2015), and NFATc3, intracellular

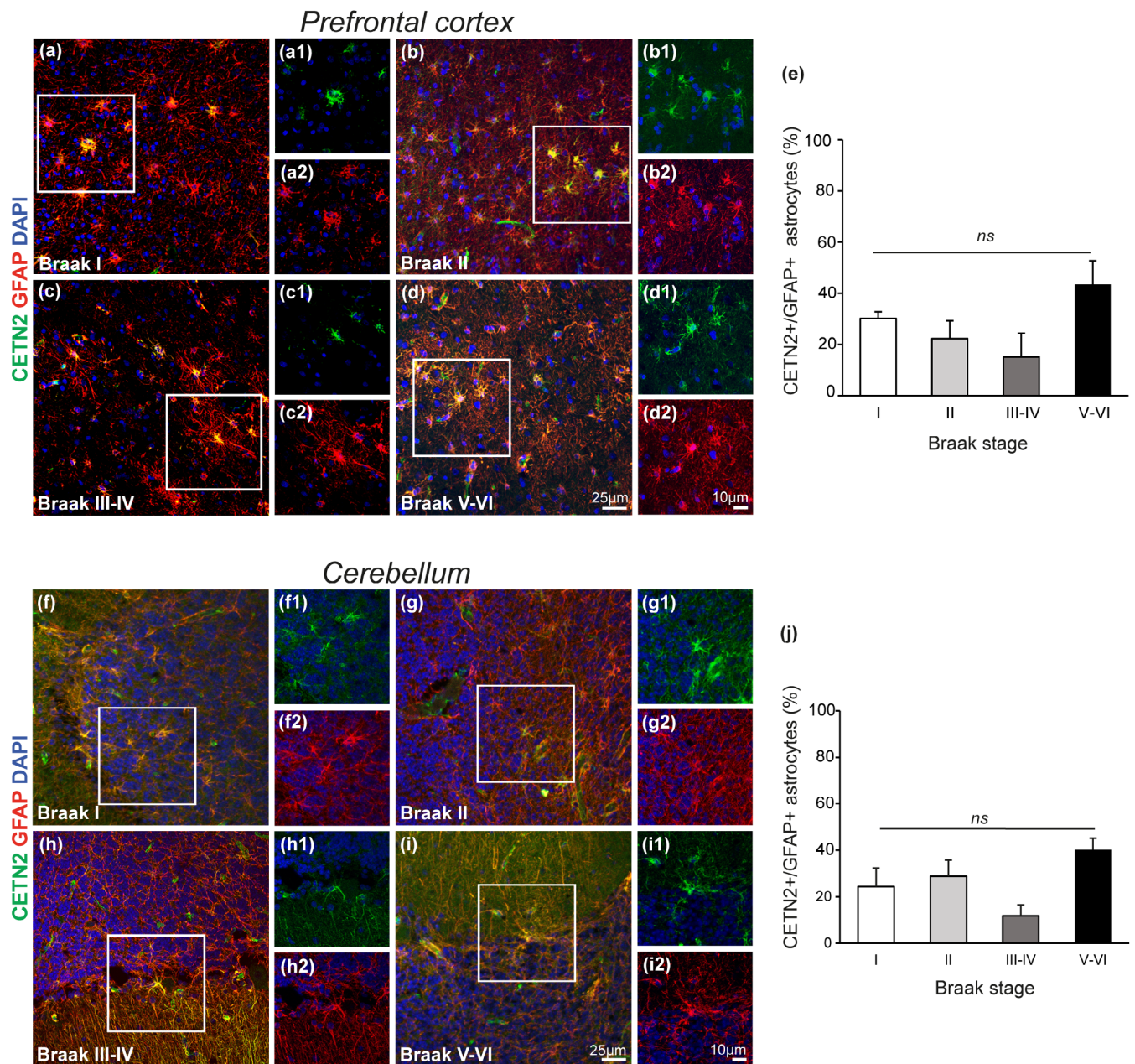


**FIGURE 2** Prefrontal cortex and cerebellar astrocytes do not exhibit variation in CETN2 expression with Alzheimer's disease progression. (a–d2) Representative images of human prefrontal cortex (a–d2) at Braak stage I (a–a2), Braak stage II (b–b2), Braak stage III–IV (c–c2), and Braak stage V–VI (d–d2) do not show significant variations of CETN2 immunopositivity. (a1–a2 to d1–d2) show magnifications of (a), (b), (c), and (d), respectively. (e) Histogram representing the percentage of CETN2+ astrocytes on the total of GFAP+ cells through all the Braak stages (Kruskal–Wallis test corrected for Dunn's test, prefrontal cortex  $p = .15$ ). (f–i2) CETN2 immunolabeling in cerebellum at Braak stage I (f–f2), Braak stage II (g–g2), Braak stage III–IV (h, h2), Braak stage V–VI (i–i2) do not indicate a variation in CETN2 signal. (f1–f2 to i1–i2) show magnifications of (f), (g), (h), and (i), respectively. (j) Histogram representing the percentage of CETN2+ astrocytes on the total of GFAP+ cells through all the Braak stages (Kruskal–Wallis test corrected for Dunn's test,  $p = .08$ ). Statistical analysis revealed no difference between Braak I and Braak V–VI samples for both prefrontal cortex and cerebellum. All histograms show mean  $\pm$  SEM. Scale bars: (a–d) and (h–i): 25  $\mu$ m; (a1–d2) and (h1–i2): 10  $\mu$ m.

mediator of calcineurin signaling (Abdul et al., 2009; Furman & Norris, 2014).

We conducted an immunofluorescence assay colabeling astrocytes in the entorhinal cortex of intermediate and severe AD patients with anti-CETN2 antibody, in combination with the anti-STAT3 or the anti-NFATc3 antibodies. We found that CETN2 labeled STAT3+

astrocytes in the most advanced AD stages, with a percentage of cells co-expressing the two markers of  $50.5\% \pm 1.8\%$  and  $71.0\% \pm 19.3\%$  in Braak III–IV and Braak V–VI samples, respectively (Figure 5a–c). Conversely, the percentage of co-expression of CETN2 and NFATc3 was estimated to be  $23.8\% \pm 6.6\%$  in Braak III–IV and  $36.0\% \pm 6.8\%$  in Braak V–VI (Figure 5d–f).



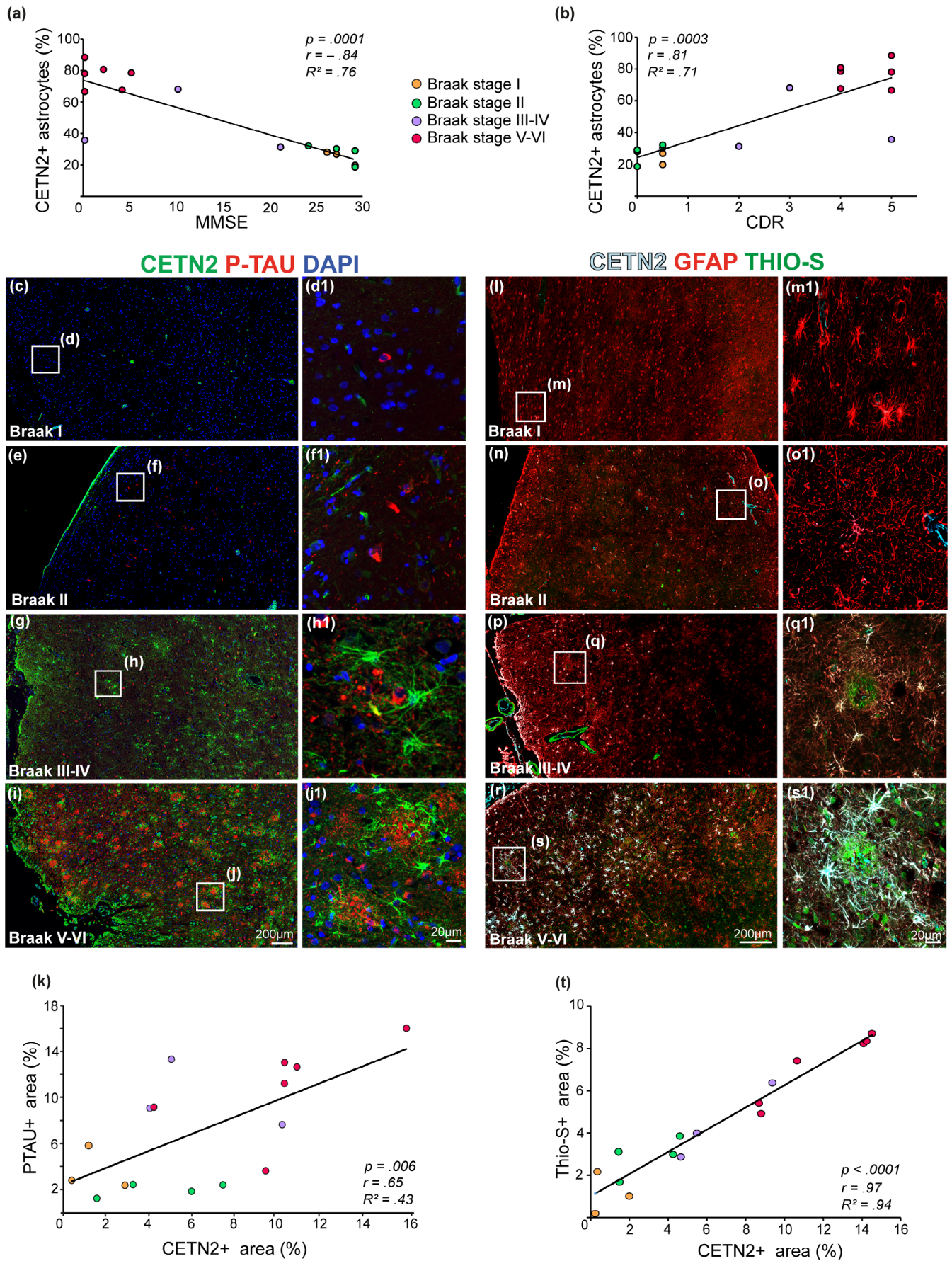
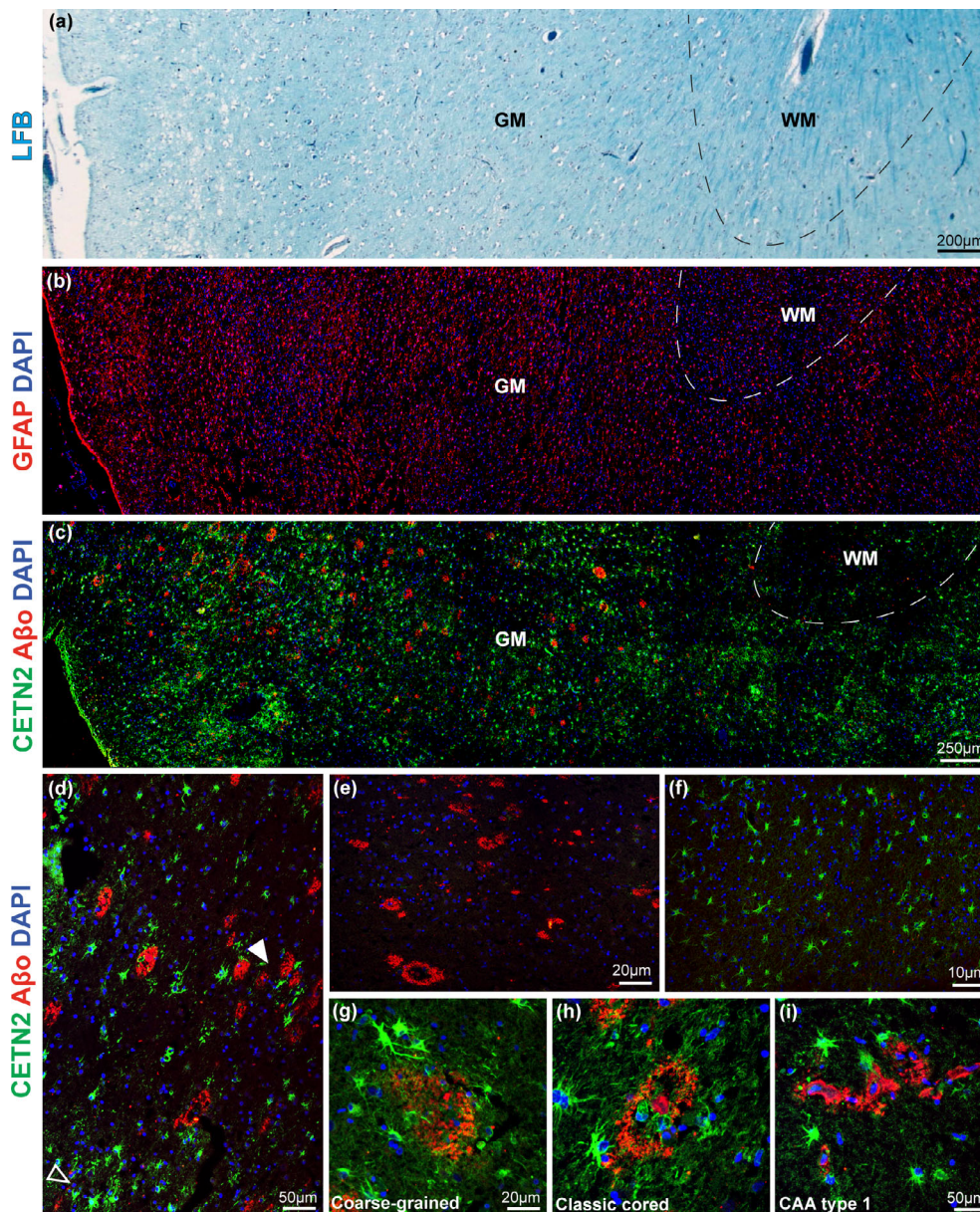


FIGURE 3 Legend on next page.





**FIGURE 4** CETN2 labeling in diseased entorhinal cortex displays a clustered pattern. (a) Human entorhinal cortex afflicted by Alzheimer's disease stained with luxol fast blue (LFB) for the identification of the gray and white matter. (b) GFAP-expressing astrocytes are uniformly distributed throughout the entorhinal cortex labeling both protoplasmic and fibrous astrocytes. (c) anti-CETN2 antibody reveals a larger abundance of CETN2-expressing astrocytes in the gray matter, where the A $\beta$  load is more abundant. Unlike GFAP, CETN2 displays a clustered distribution. (d) Within the same area, CETN2+ astrocytes can be found either juxtaposed to plaques (full arrow) or dispersed in the parenchyma (empty arrow). (e) A $\beta$  plaques not surrounded by CETN2+ astrocytes. (f) CETN2+ astrocytes without the presence of A $\beta$  plaques. (g–i) Immunostaining illustrating the arrangement of CETN2+ astrocytes in proximity of diverse amyloid aggregates: coarse-grained and classic cored-plaques and around a brain capillary affected by CAA type 1. Scale bars: (a): 200  $\mu$ m; (b and c): 250  $\mu$ m; (d): 50  $\mu$ m; (e): 20  $\mu$ m; (f): 10  $\mu$ m; (g): 20  $\mu$ m; (h and i): 50  $\mu$ m.

Growing research has focused on a new cerebrospinal fluid (CSF) biomarker YKL-40, a glycoprotein commonly measured as a neuroinflammation parameter in AD, and histologically expressed in astrocytes

(Craig-Schapiro et al., 2010; Moreno-Rodriguez et al., 2020; Querol-Vilaseca et al., 2017; Zhang et al., 2018). In our samples, a large degree of overlap was observed when CETN2+ astrocytes were counterstained for

**FIGURE 3** CETN2+ astrocyte abundance correlates with cognitive decline and neuropathological Alzheimer's disease hallmarks. (a) Graph showing the negative correlation between the mini mental state examination (MMSE) score and the percentage of CETN2+ astrocytes in the entorhinal cortex (Spearman correlation analysis,  $p = .0001$ ;  $r = -.84$ ;  $R^2 = .76$ ). (b) Graph showing the positive correlation between the clinical dementia rating (CDR) score and the CETN2 immunoreactivity in the entorhinal cortex (Spearman correlation analysis,  $p = .0003$ ;  $r = .81$ ;  $R^2 = .71$ ). (c–f1) Double staining for p-TAU (in red) and CETN2 (in green) uncovers the deficiency of both neurofibrillary tangle (NFT) deposits and CETN2+ astrocytes in entorhinal cortices in Braak stage I–II. (g–j1) The load of NFTs increases in association with a large number of CETN2 immunoreactive astroglia in Braak III–IV and V–VI. (k) Correlation graph showing the percentage of pTAU+ areas and CETN2+ areas across all samples (Pearson correlation analysis,  $p = .006$ ,  $r = .65$ ,  $R^2 = 0.43$ ). (l–o1) Immunofluorescence analysis of amyloid deposition, revealed by thio-S immunoreactivity (green), and CETN2+ astrocytes (light blue) at Braak stage I–II. Astrocytes express GFAP (red), but CETN2 expression is scarcely detectable. (p–q1) At Braak stage III–IV CETN2 immunopositivity of astrocytes increases noticeably reaching the highest signal in Braak V–VI ( $r = s1$ ) with the deposition of A $\beta$  plaques. Astrocytes morphology is suggestive of an ongoing reactive state. (t) The increase in CETN2+ area, in percentage, positively correlates with the percentage thio-S+ area (Pearson correlation analysis,  $p < .0001$ ,  $r = .97$ ,  $R^2 = .94$ ). Scale bars: (c–r): 200  $\mu$ m; (d1–s1): 20  $\mu$ m.



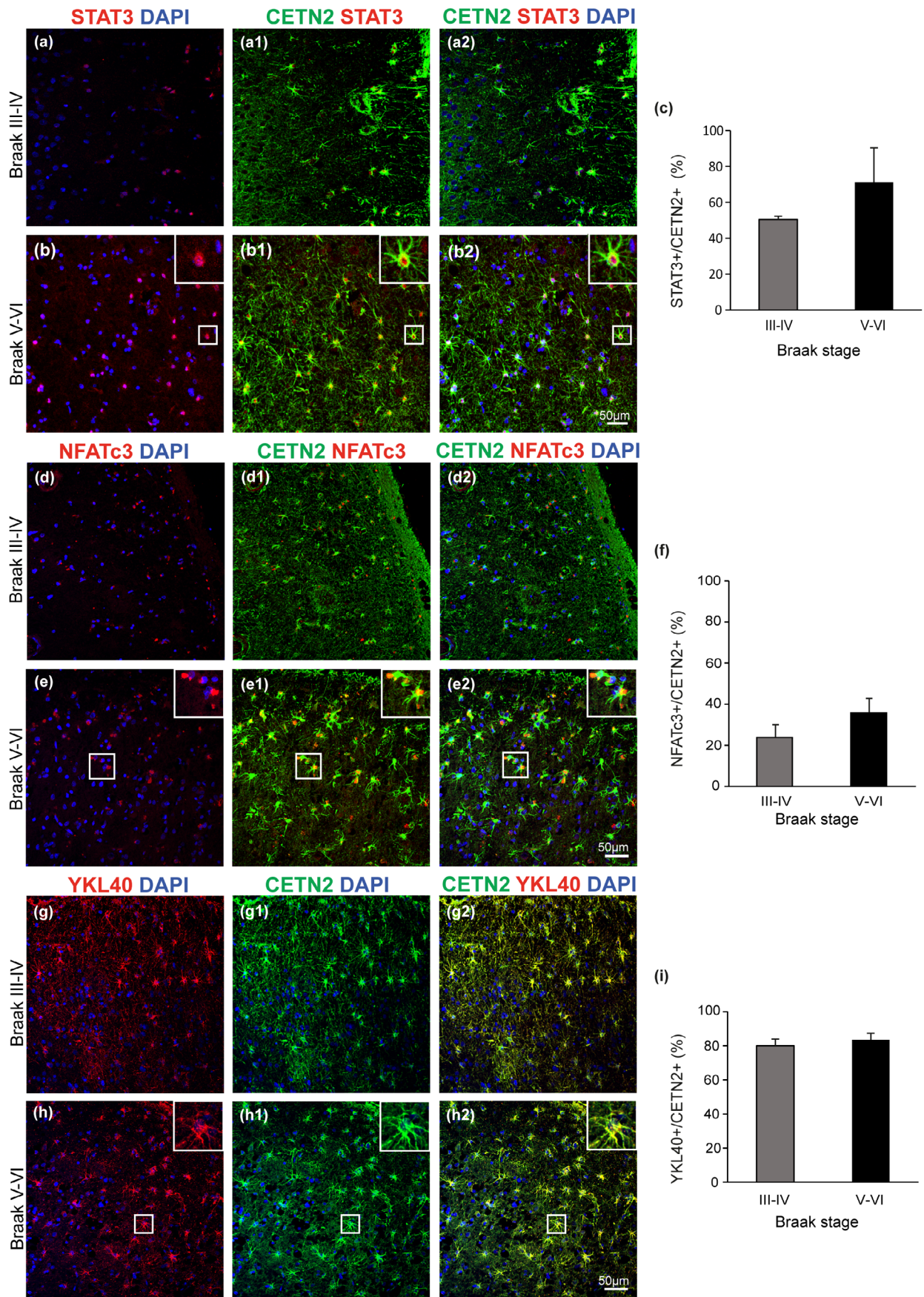


FIGURE 5 Legend on next page.

YKL40. Specifically,  $80.0\% \pm 4.0\%$  of CETN2+ astrocytes also exhibited YKL40 cytoplasmic immunopositivity in Braak III–IV stage samples, a percentage that increased to  $83.6\% \pm 3.9\%$  in Braak V–VI (Figure 5g–i).

Collectively, these data indicate that in the entorhinal cortex, CETN2 undergoes a significant increase in expression within astrocytes, and which directly correlates with the two most typical neuropathological lesions of the AD affected brain, similarly to other annotated reactive glia markers.

## 4 | DISCUSSION

Understanding the role of astrocytes is increasingly important to shed light on the pathophysiology of brain diseases and of AD in particular (Endo et al., 2022). Heterogeneity in astrocytic functions is related to their anatomical location, and astrocytes within different subcellular or synaptic compartments may exhibit diverse signaling and/or protein expression. Moreover, brain lesions can cause astrocytic modifications depending on the nature of the injury leading to diverse phenotypic, morphological, and functional changes (Khakh & Sofroniew, 2015).

In this framework, we have recently discovered that the centrosomal protein CETN2 is also present in the cytoplasm of human astrocytes with a variable distribution depending on the anatomical site (Degl'Innocenti et al., 2022). Other studies have pointed out that astrocyte proteins, such as GFAP, S100B, BLBP, or vimentin (Gotz et al., 2015) are subject to variation in their expression concomitantly with the initiation of a reactive state, also featured by peculiar morphological changes (Escartin et al., 2021). In this study, we sought to determine whether the astrocytic expression of CETN2 is also altered in neurodegenerative conditions and focused our attention on AD, as the most frequent neurodegenerative disease.

The analysis was performed on brains from a cohort of 16 subjects, for which a complete clinical profile was obtained *ante mortem*. Our results indicated a strong correlation between astrocyte CETN2 immunoreactivity and worsening cognitive abilities, as well as with the abundance of cardinal AD lesions (P-TAU and amyloid load). Interestingly, this peculiar profile in CETN2 expression was limited to the entorhinal cortex, an area early affected by the disease and otherwise poor in CETN2+ astrocytes in the healthy brain (Degl'Innocenti et al., 2022). Although the study has limitations regarding the number of cases included, the statistical power of the investigated cohort was confirmed. The sample size originated from restrictive inclusion criteria based on the clinical diagnosis and *post mortem* neuropathological assessment. Only cases exhibiting an almost pure AD pathology

were selected with neurological comorbidities limited to cerebrovascular disease. Samples reporting neuro-oncological conditions were deliberately excluded, as well as samples with a *post mortem* interval exceeding 20 h. Additionally, the observations were corroborated by three different technical approaches, all of which highlighted progressive CETN2 astrocytic expression with Braak staging: immunoblot and immunohistochemistry served for a preliminary exploration of the three anatomical areas, while targeted mass spectrometry was performed as an antibody-independent validation method.

Immunofluorescence assays indicated that CETN2 labeling was mostly prevalent in protoplasmic astrocytes of the entorhinal gray matter and appeared dispersed in the parenchyma, adjacent to plaques or in areas free of amyloid burden, with a clumped distribution that differed from the uniform pattern of GFAP. Although a number of CETN2+ astrocytes appeared to be attracted by NPs, their presence in plaques-free areas is indicative of a multifactorial causality at the origin of CETN2 expression. The spatial distance of CETN2+ astrocytes from lesions may be due to the local release of factors from microglia cells (Ben Haim, Carrillo-de Sauvage, et al., 2015), together with the local phagocytosis of A $\beta$  peptides that may anticipate the formation of immunohistochemically detectable plaques. Additionally, we found that CETN2 exhibits human-specific expression in AD. This finding aligns with previous research highlighting physiological differences between human and murine astrocytes (Zhang et al., 2016, Degl'Innocenti et al., 2022), and here we show that these differences are also evident in pathological contexts. Indeed, gene expression patterns of reactive astrocytes often show poor concordance between mice and humans in the neurodegenerative context, thus indicating that the murine counterpart cannot fully replicate the complexity of human diseases like AD (Das et al., 2020).

The concomitant expression of other annotated reactive glia markers such as STAT3, NFATc3, and YKL-40 suggests that CETN2 may participate in the glial activation process. The larger percentage of CETN2+/STAT3+ astrocytes compared with CETN2+/NFATc3+ astrocytes could be indicative of a preponderant participation of CETN2 in the JAK/STAT3-mediated cascade for the initiation or maintenance of a reactive state, without excluding a STAT3-mediated CETN2 transcription, as shown for other reactive glia proteins (Ben Haim, Carrillo-de Sauvage, et al., 2015). We observed that the greatest percentage of immunolabeling overlap was observed between CETN2 and YKL-40, a more recently discovered astrocyte protein whose function has not been fully elucidated (Querol-Vilaseca et al., 2017). Similar to CETN2, YKL40+ astrocytes have also been described close to amyloid deposits and far from them (Moreno-Rodriguez et al., 2020), thus

**FIGURE 5** CETN2 labels reactive astrocytes in Alzheimer's disease-affected entorhinal cortices: (a–b2) Immunostainings showing nuclear STAT3 and cytoplasmic CETN2 in Braak stage III–IV and Braak stage V–VI indicating the presence of reactive astrocytes. (c) Histogram showing the percentage of STAT3+ nuclei over the total number of CETN2+ astrocytes in Braak stage III–IV and Braak stage V–VI. (d–e2) Immunofluorescence labeling for NFATc3 and CETN2 in Braak stage III–IV and V–VI entorhinal cortices. (f) Histogram indicates the percentage of NFATc3+ astrocytes on the total of CETN2+ astrocytes. (g–h2) Immunofluorescence staining for YKL40 showing the overlap with CETN2 cytosolic signal. (i) Histograms represents YKL40+ astrocytes on the total of CETN2+ in percentage. All histograms represent mean  $\pm$  SEM. Scale bars: 50  $\mu$ m.



indicating that the expression of both proteins may undergo regulation mechanisms other than direct A $\beta$  exposure. YKL-40 has also been found in liquid biopsies, including human plasma at the earliest stages of AD (Craig-Schapiro et al., 2010; Zhang et al., 2018) and in the CSF of predementia subjects together with other inflammatory proteins (sTREM2, sAXL, sTyro3, MIF, complement factors C1q, C4, and H, ferritin, and ApoE) (Brosseron et al., 2022). Further analyses will be necessary to clarify whether CETN2 and YKL-40 expression is triggered by a shared intracellular pathway and whether, similar to YKL-40, CETN2 can be released in CSF and plasma before symptoms become clinically detectable.

A direct comparison with other astroglial proteins, that is, GFAP (Duffy et al., 1980), S100B (Mrak & Griffin, 2001) and MAO-B (Jaisa-Aad et al., 2024), whose expression is impacted by AD initiation, highlights similarities, and differences with CETN2. For instance, a progressive increase in the expression of S100B reported in AD cases (Mrak et al., 1996) has also been observed along with the normal aging process (Mrak & Griffin, 2005). In our cohort, CETN2 was detected in the entorhinal cortices of NOLD individuals, becoming progressively more appreciable only in patients with AD and did not show correlation with age, thus suggesting that, unlike S100B, the entorhinal expression of CETN2 is more strictly associated with disease progression. Nevertheless, additional investigations with larger cohorts of patients will be needed to corroborate this observation.

GFAP has been reported as a trusted marker of astrocyte reactivity in AD (Kumar et al., 2023) as its expression positively correlates with disease progression and an increased number of NFTs (Serrano-Pozo et al., 2011). However, due to its variable distribution across brain regions, GFAP is unlikely to serve as an absolute indicator of astrogliosis. Rodent data indicate that in the hippocampus, one of the first areas to be affected by AD, about 40% of astrocytes are S100B-positive and GFAP-negative (Ogata & Kosaka, 2002). Comparably, CETN2 is not uniformly distributed in the brain (Degl'Innocenti et al., 2022) and, based on our findings, its increase in expression with AD is also spatially confined. However, the variation of GFAP and CETN2 expression with disease progression is different: while GFAP provides the initial footprint of astrocyte reactivity, CETN2 may belong to the second wave of reactive astrocyte markers, detectable in the advanced stages of AD dementia (Kumar et al., 2023). Furthermore, GFAP is a well-established marker of astrogliosis found in various neurodegenerative diseases, not only in AD (Heimfarth et al., 2022). Therefore, it raises the question of whether CETN2 expression is unique to AD or, like GFAP, is a general neuroinflammatory marker common to other neuropathological conditions. Future investigations involving diverse patient cohorts will be necessary to determine its suitability as a specific disease marker.

MAO-B is also another marker of reactivity and, at present, its relative PET radiotracer <sup>11</sup>C-deuterium-L-deprenyl (DED) (Fontana et al., 2023) proved to be efficient for the detection of prodromal AD (Carter et al., 2012). Of note, evidence has shown that MAO-B and GFAP do not colocalize and, unlike CETN2, its signal becomes stronger in prefrontal and parietal cortices of affected individuals. Considering the high variability in the spatio-temporal expression of these

glial proteins, no indication currently supports the eligibility of one single protein as a gold-standard marker for AD-astrogliosis and, at present, a combination of markers, rather than a single one, may be more informative of disease progression.

Our immunoblot analysis on entorhinal cortices suggested the presence of a modified form of CETN2 with an apparent molecular weight of 25 kDa. In-gel proteolytic digestion followed by LC-MS/MS analysis of human rCETN2 enabled the identification of PTMs in the 25 kDa CETN2 band, namely acetylation of lysine 30 and carbamylation of lysine 22 and 103. Among PTMs, acetylation has a considerable impact on vital biological processes; the addition of acetyl groups to proteins regulates function and viability in mammalian cells, and it has been linked to the pathogenesis of neurodegenerative diseases (Adav & Sze, 2020; Kabir et al., 2022). Similarly, carbamylation has been detected in Tau and  $\alpha$ -synuclein, inducing protein aggregation, cellular dysfunction, and neuronal toxicity (Gallart-Palau et al., 2017; Guru KrishnaKumar et al., 2018), and has been linked to aging, the primary risk factor for AD (Thal et al., 2016). Carbamylation can occur either enzymatically or nonenzymatically in vivo (George et al., 1960; Wang et al., 2007) and evidence shows that the addition of a cyanate group may produce an alteration of the protein's Stokes radius, causing a shift in the migration behavior of proteins on polyacrylamide gels, similar to what is observed for CETN2 (Adav & Sze, 2020; Gallart-Palau et al., 2017). Our LC-MS/MS analysis achieved high sequence coverage for human rCETN2 (81.4% of the 20 kDa band and 76.6% of the 25 kDa band), however it did not include the C-terminal peptide whose phosphorylation on serine 170 was previously associated with an up-shifted electrophoretic band for CETN2 (Lutz et al., 2001). Therefore, it can be speculated that a combination of PTMs other than carbamylation and acetylation reported in our study could contribute to the apparent 25 kDa band of CETN2 detected in the biochemical assays. Quantitative proteomics in support of stereological and biochemical assays was also performed, and it confirmed the increment on CETN2 expression along Braak staging for both the native and modified form of the protein.

Additional investigations will be necessary to elucidate the potential function of CETN2 in astrocyte biology, but assumptions can be made. CETN2 is annotated as a calcium-binding protein and, while its presence in human astrocytes has only been recently outlined (Degl'Innocenti et al., 2022), its cellular localization agrees with the plethora of functions operated by calcium for astrocytic signaling (Verkhatsky, 2019). Astrocyte calcium is regulated by a diverse set of stimuli, including A $\beta$ , which can alter its intracellular levels (Adav & Sze, 2020; Delekate et al., 2014; Fontana et al., 2023; Gabbouj et al., 2019; Gallart-Palau et al., 2017; George et al., 1960; Guru KrishnaKumar et al., 2018; Heimfarth et al., 2022; Kabir et al., 2022; Lutz et al., 2001; Ogata & Kosaka, 2002; Ren et al., 2019; Thal et al., 2016; Wang et al., 2007). The native conformation of CETN2, with four EF-hand calcium binding domains, is very similar to other calcium sensors (Berridge et al., 2000), and a comparable function can be speculated. As demonstrated by the clear differences in topographical distribution, it is very likely that CETN2+ astrocytes perform different functions and have different interactions with microglia and

neurons in physiological conditions and in reaction to pathology. These interesting aspects remain to be explored.

Collectively, our results delineate the detailed distribution of CETN2+ astrocytes in the human entorhinal cortex and point out a strong correlation between its expression and AD cognitive dysfunction and histopathological lesions. The copresence of other reactive glia markers in CETN2+ astrocytes indicates the participation of CETN2 in astrogliosis processes, although the exact mechanisms that trigger its expression remain to be determined. As very recently outlined (Guo et al., 2024), astrocytic proteins detectable in the plasma have a strong predictive value in determining the risk of developing AD and this encourages further efforts toward an accurate understanding of astrocyte function and the identification of molecular markers underpinning their vast heterogeneity.

### AUTHOR CONTRIBUTIONS

E.D.I. performed immunohistochemistry experiments, confocal microscopy, stereological, and statistical analyses, prepared figures and figure legends, and contributed to the writing of the manuscript. T.E.P. performed patients' clinical and neuropathological characterization, surgical brain removal, and sampling, and contributed to data interpretation and writing of the manuscript. V.M. assisted in surgical brain removal, performed brain fixation, sectioning and histological assays, and contributed to neuropathological characterization. F.O. performed western blot and quantifications. F.F. performed targeted mass spectrometry on brain lysates and their quantification. X.P. assisted in brain sampling, sectioning, and histological assays. C.M. purified recombinant CETN2 from *E. Coli*. A.P. performed statistical power analysis. C.E. and K.B. provided and analyzed mouse samples. L.A.M.D. supervised mass spectrometry analyses, contributed to data interpretation, and revised the final manuscript. M.T.D.A. conceived the experiments, supervised experimentation and data analyses, and wrote the manuscript.

### ACKNOWLEDGMENTS

We thank Dr. Laura Salvini, Dr. Laura Tinti, Dr. Vittoria Cicaloni from Toscana Life Science (TLS) for CETN2 post-translational modifications analyses. We are grateful to Prof. Mauro Ceroni and Dr. Antonio Guaita for reading the manuscript. We thank Drs. Kelly Ceyzériat and Océane Guillemaud for help in generating 3xTg and APP/PS1dE9 mouse brain sections, respectively. We thank Dr. Hélène Hirbec (IGF, Montpellier) for providing APP<sup>NL-F/NL-F</sup> mice and Dr. Takashi Saito and for sharing these mice.

### FUNDING INFORMATION

This work was supported under FPS Grant 2018 (to MTD'A), by CUP B13D21011850006 PNRR MUR–M4C2–ECS00000017 “THE–TUSCANY HEALTH ECOSYSTEM” (to Fondazione Pisana per la Scienza ONLUS), by Fondo Beneficenza Intesa San Paolo–Brain Bank Project B-2022-0094 (to Fondazione Golgi-Cenci). The mouse study was supported by ANR (TRANS3; #ANR21-CE17-0047-02) (to CE). The funders of the study had no role in the study design, data collection, data analysis, data interpretation, or writing of the report.

### CONFLICT OF INTEREST STATEMENT

The authors declare that the research was conducted in the absence of any commercial or financial relationships that could be construed as a potential conflict of interest.

### DATA AVAILABILITY STATEMENT

The data that support the findings of this study are available from the corresponding author upon reasonable request.

### INFORMED CONSENT

The authors of this research confirm that an informed consent has been obtained from each participant, comprising samples' harvesting and analysis, and publication of results. All the cases have been coded and anonymized, and the images show only histologic microphotographs; thus, the recognition of the patients' identity is not possible. Consent for clinical assessment, brain donation and storage, neuropathological assessment and data use for research was obtained in accordance with the Ethic Committee of the University of Pavia on 6 October 2009 (Committee report 3/2009) within the Invece.Ab project. The consent form was judged by our Internal Review Board as complete and easily comprehensible. ABB donation program includes cognitively normal elderly individuals and patients affected by NCD. Joining the brain donation program was a personal decision requiring complete awareness. In case a donor was not deemed competent to sign the consent form, authorization from a legal guardian or next-of-kin was warranted, taking into account the wishes previously expressed by the subject.

### ORCID

Elisa Degl'Innocenti  <https://orcid.org/0000-0002-3819-0116>  
Tino Emanuele Poloni  <https://orcid.org/0000-0002-8463-6879>  
Valentina Medici  <https://orcid.org/0000-0001-9385-3384>  
Francesco Olimpico  <https://orcid.org/0009-0003-0392-2983>  
Francesco Finamore  <https://orcid.org/0009-0005-7875-662X>  
Xhulja Profka  <https://orcid.org/0000-0002-5785-3325>  
Karouna Bascarane  <https://orcid.org/0009-0005-5764-8275>  
Castrese Morrone  <https://orcid.org/0000-0002-3993-7306>  
Aldo Pastore  <https://orcid.org/0009-0007-3037-0474>  
Carole Escartin  <https://orcid.org/0000-0003-3613-4118>  
Liam A. McDonnell  <https://orcid.org/0000-0003-0595-9491>  
Maria Teresa Dell'Anno  <https://orcid.org/0000-0003-1825-671X>

### REFERENCES

- Abdul, H. M., Sama, M. A., Furman, J. L., Mathis, D. M., Beckett, T. L., Weidner, A. M., Patel, E. S., Baig, I., Murphy, M. P., LeVine, H., 3rd, Kraner, S. D., & Norris, C. M. (2009). Cognitive decline in Alzheimer's disease is associated with selective changes in calcineurin/NFAT signaling. *The Journal of Neuroscience*, 29(41), 12957–12969.
- Acosta, C., Anderson, H. D., & Anderson, C. M. (2017). Astrocyte dysfunction in Alzheimer disease. *Journal of Neuroscience Research*, 95(12), 2430–2447.
- Adav, S. S., & Sze, S. K. (2020). Hypoxia-induced degenerative protein modifications associated with aging and age-associated disorders. *Aging and Disease*, 11(2), 341–364.

- Arranz, A. M., & De Strooper, B. (2019). The role of astroglia in Alzheimer's disease: Pathophysiology and clinical implications. *Lancet Neurology*, 18(4), 406–414.
- Association AP. *Diagnostic and statistical manual of mental disorders (DSM-5)*. American Psychiatric Publishing, 2013.
- Beach, T. G., White, C. L., 3rd, Hladik, C. L., Sabbagh, M. N., Connor, D. J., Shill, H. A., Sue, L. I., Sasse, J., Bachalakuri, J., Henry-Watson, J., Akiyama, H., & Adler, C. H. (2009). Olfactory bulb alpha-synucleinopathy has high specificity and sensitivity for Lewy body disorders. *Acta Neuropathologica*, 117(2), 169–174.
- Ben Haim, L., Carrillo-de Sauvage, M. A., Ceyzeriat, K., & Escartin, C. (2015). Elusive roles for reactive astrocytes in neurodegenerative diseases. *Frontiers in Cellular Neuroscience*, 9, 278.
- Ben Haim, L., Ceyzeriat, K., Carrillo-de Sauvage, M. A., Aubry, F., Auregan, G., Guillermier, M., Ruiz, M., Petit, F., Houitte, D., Faivre, E., Vandesquille, M., Aron-Badin, R., Dhenain, M., Déglon, N., Hantraye, P., Brouillet, E., Bonventon, G., & Escartin, C. (2015). The JAK/STAT3 pathway is a common inducer of astrocyte reactivity in Alzheimer's and Huntington's diseases. *The Journal of Neuroscience*, 35(6), 2817–2829.
- Berridge, M. J., Lipp, P., & Bootman, M. D. (2000). The versatility and universality of calcium signalling. *Nature Reviews. Molecular Cell Biology*, 1(1), 11–21.
- Boon, B. D. C., Bulk, M., Jonker, A. J., Morrema, T. H. J., van den Berg, E., Popovic, M., Walter, J., Kumar, S., van der Lee, S. J., Holstege, H., Zhu, X., van Nostrand, W. E., Natté, R., van der Weerd, L., Bouwman, F. H., van de Berg, W. D. J., Rozemuller, A. J. M., & Hoozemans, J. J. M. (2020). The coarse-grained plaque: A divergent Abeta plaque-type in early-onset Alzheimer's disease. *Acta Neuropathologica*, 140(6), 811–830.
- Braak, H., Alafuzoff, I., Arzberger, T., Kretschmar, H., & Del Tredici, K. (2006). Staging of Alzheimer disease-associated neurofibrillary pathology using paraffin sections and immunocytochemistry. *Acta Neuropathologica*, 112(4), 389–404.
- Brosseron, F., Maass, A., Kleinedam, L., Ravichandran, K. A., González, P. G., McManus, R. M., Ising, C., Santarelli, F., Kolbe, C. C., Häslér, L. M., Wolfsgruber, S., Marquié, M., Boada, M., Orellana, A., de Rojas, I., Röske, S., Peters, O., Cosma, N. C., Cetindag, A., ... DELCODE study group. (2022). Soluble TAM receptors sAXL and sTyro3 predict structural and functional protection in Alzheimer's disease. *Neuron*, 110(6), 1009–1022.e4.
- Carter, S. F., Schöll, M., Almkvist, O., Wall, A., Engler, H., Långström, B., & Nordberg, A. (2012). Evidence for astrocytosis in prodromal Alzheimer disease provided by 11C-deuterium-L-deprenyl: A multitracier PET paradigm combining 11C-Pittsburgh compound B and 18F-FDG. *Journal of Nuclear Medicine*, 53(1), 37–46.
- Ceyzeriat, K., Ben Haim, L., Denizot, A., Pommier, D., Matos, M., Guillemaud, O., Palomares, M. A., Abjean, L., Petit, F., Gipchtein, P., Gaillard, M. C., Guillermier, M., Bernier, S., Gaudin, M., Aurégan, G., Joséphine, C., Déchamps, N., Veran, J., Langlais, V., ... Escartin, C. (2018). Modulation of astrocyte reactivity improves functional deficits in mouse models of Alzheimer's disease. *Acta Neuropathologica Communications*, 6(1), 104.
- Chun, H., Im, H., Kang, Y. J., Kim, Y., Shin, J. H., Won, W., Lim, J., Ju, Y., Park, Y. M., Kim, S., Lee, S. E., Lee, J., Woo, J., Hwang, Y., Cho, H., Jo, S., Park, J. H., Kim, D., Kim, D. Y., ... Lee, C. J. (2020). Severe reactive astrocytes precipitate pathological hallmarks of Alzheimer's disease via H<sub>2</sub>O<sub>2</sub><sup>-</sup> production. *Nature Neuroscience*, 23(12), 1555–1566.
- Chun, H., & Lee, C. J. (2018). Reactive astrocytes in Alzheimer's disease. A double-edged sword. *Neuroscience Research*, 126, 44–52.
- Craig-Schapiro, R., Perrin, R. J., Roe, C. M., Xiong, C., Carter, D., Cairns, N. J., Mintun, M. A., Peskind, E. R., Li, G., Galasko, D. R., Clark, C. M., Quinn, J. F., D'Angelo, G., Malone, J. P., Townsend, R. R., Morris, J. C., Fagan, A. M., & Holtzman, D. M. (2010). YKL-40: A novel prognostic fluid biomarker for preclinical Alzheimer's disease. *Biological Psychiatry*, 68(10), 903–912.
- Cummings, J., Zhou, Y., Lee, G., Zhong, K., Fonseca, J., & Cheng, F. (2023). Alzheimer's disease drug development pipeline: 2023. *Alzheimers Dement*, 9(2), e12385. <https://doi.org/10.1002/trc2.12385>. Erratum in: *Alzheimers Dement* (2023), 9(2), e12407.
- Das, S., Li, Z., Noori, A., Hyman, B. T., & Serrano-Pozo, A. (2020). Meta-analysis of mouse transcriptomic studies supports a context-dependent astrocyte reaction in acute CNS injury versus neurodegeneration. *Journal of Neuroinflammation*, 17(1), 227.
- Degl'Innocenti, E., Poloni, T. E., Medici, V., Recupero, L., Dell'Amico, C., Vannini, E., Borello, U., Mazzanti, C. M., Onorati, M., & Dell'Anno, M. T. (2022). Centrin 2: A novel marker of mature and neoplastic human astrocytes. *Frontiers in Cellular Neuroscience*, 16, 858347.
- Delekate, A., Fuchtemeier, M., Schumacher, T., Ulbrich, C., Foddiss, M., & Petzold, G. C. (2014). Metabotropic P2Y1 receptor signalling mediates astrocytic hyperactivity in vivo in an Alzheimer's disease mouse model. *Nature Communications*, 5, 5422.
- Dooneief, G., Marder, K., Tang, M. X., & Stern, Y. (1996). The clinical dementia rating scale: Community-based validation of "profound" and "terminal" stages. *Neurology*, 46(6), 1746–1749.
- Duffy, P. E., Rapport, M., & Graf, L. (1980). Glial fibrillary acidic protein and Alzheimer-type senile dementia. *Neurology*, 30(7 Pt 1), 778–782.
- Endo, F., Kasai, A., Soto, J. S., Yu, X., Qu, Z., Hashimoto, H., Gradinaru, V., Kawaguchi, R., & Khakh, B. S. (2022). Molecular basis of astrocyte diversity and morphology across the CNS in health and disease. *Science*, 378(6619), eadc9020.
- Escartin, C., Galea, E., Lakatos, A., O'Callaghan, J. P., Petzold, G. C., Serrano-Pozo, A., Steinhäuser, C., Volterra, A., Carmignoto, G., Agarwal, A., Allen, N. J., Araque, A., Barbeito, L., Barzilai, A., Bergles, D. E., Bonvento, G., Butt, A. M., Chen, W.-T., Cohen-Salmon, M., ... Verkhratsky, A. (2021). Reactive astrocyte nomenclature, definitions, and future directions. *Nature Neuroscience*, 24(3), 312–325.
- Fakhoury, M. (2018). Microglia and astrocytes in Alzheimer's disease: Implications for therapy. *Current Neuropharmacology*, 16(5), 508–518.
- Fontana, I. C., Scarpa, M., Malarte, M. L., Rocha, F. M., Ausellé-Bosch, S., Bluma, M., Bucci, M., Chiotis, K., Kumar, A., & Nordberg, A. (2023). Astrocyte signature in Alzheimer's disease continuum through a multi-PET tracer imaging perspective. *Cells*, 12(11), 1469.
- Frost, G. R., & Li, Y. M. (2017). The role of astrocytes in amyloid production and Alzheimer's disease. *Open Biology*, 7(12), 170228.
- Furman, J. L., & Norris, C. M. (2014). Calcineurin and glial signaling: Neuroinflammation and beyond. *Journal of Neuroinflammation*, 11, 158.
- Gabbouj, S., Ryhänen, S., Marttinen, M., Wittrahm, R., Takalo, M., Kempainen, S., Martiskainen, H., Tanila, H., Haapasalo, A., Hiltunen, M., & Natunen, T. (2019). Altered insulin signaling in Alzheimer's disease brain—Special emphasis on PI3K-Akt pathway. *Frontiers in Neurosciences*, 13, 629.
- Gallart-Palau, X., Serra, A., Lee, B. S. T., Guo, X., & Sze, S. K. (2017). Brain ureido degenerative protein modifications are associated with neuroinflammation and proteinopathy in Alzheimer's disease with cerebrovascular disease. *Journal of Neuroinflammation*, 14(1), 175.
- Garcia-Marin, V., Garcia-Lopez, P., & Freire, M. (2007). Cajal's contributions to the study of Alzheimer's disease. *Journal of Alzheimer's Disease*, 12(2), 161–174.
- George, R., Stark, W. H. S., & Moore, S. (1960). Reactions of the cyanate present in aqueous urea with amino acids and proteins. *Journal of Biological Chemistry*, 235(11), 3177–3181.
- Gotz, M., Sirko, S., Beckers, J., & Imler, M. (2015). Reactive astrocytes as neural stem or progenitor cells: In vivo lineage, in vitro potential, and genome-wide expression analysis. *Glia*, 63(8), 1452–1468.
- Guaita, A., Colombo, M., Vaccaro, R., Fossi, S., Vitali, S. F., Forloni, G., Polito, L., Davin, A., Ferretti, V. V., & Villani, S. (2013). Brain aging and dementia during the transition from late adulthood to old age: Design



- and methodology of the "Invece.Ab" population-based study. *BMC Geriatrics*, 13, 98.
- Guo, Y., You, J., Zhang, Y., Liu, W. S., Huang, Y. Y., Zhang, Y. R., Zhang, W., Dong, Q., Feng, J. F., Cheng, W., & Yu, J. T. (2024). Plasma proteomic profiles predict future dementia in healthy adults. *Nature Aging*, 4, 247–260.
- Guru KrishnaKumar, V., Baweja, L., Ralhan, K., & Gupta, S. (2018). Carboxylation promotes amyloidogenesis and induces structural changes in Tau-core hexapeptide fibrils. *Biochimica et Biophysica Acta - General Subjects*, 1862(12), 2590–2604.
- Hampel, H., Hardy, J., Blennow, K., Chen, C., Perry, G., Kim, S. H., Villemagne, V. L., Aisen, P., Vendruscolo, M., Iwatsubo, T., Masters, C. L., Cho, M., Lannfelt, L., Cummings, J. L., & Vergallo, A. (2021). The amyloid-beta pathway in Alzheimer's disease. *Molecular Psychiatry*, 26(10), 5481–5503.
- Heimfarth, L., Passos, F. R. S., Monteiro, B. S., Araújo, A. A. S., Quintans Júnior, L. J., & Quintans, J. S. S. (2022). Serum glial fibrillary acidic protein is a body fluid biomarker: A valuable prognostic for neurological disease. *International Immunopharmacology*, 107, 108624.
- Heyman, A., Wilkinson, W. E., Hurwitz, B. J., Helms, M. J., Haynes, C. S., Utley, C. M., & Gwyther, L. P. (1987). Early-onset Alzheimer's disease: Clinical predictors of institutionalization and death. *Neurology*, 37(6), 980–984.
- Hughes, C. P., Berg, L., Danziger, W. L., Coben, L. A., & Martin, R. L. (1982). A new clinical scale for the staging of dementia. *The British Journal of Psychiatry*, 140, 566–572.
- Jaisa-Aad, M., Muñoz-Castro, C., Healey, M. A., Hyman, B. T., & Serrano-Pozo, A. (2024). Characterization of monoamine oxidase-B (MAO-B) as a biomarker of reactive astrogliosis in Alzheimer's disease and related dementias. *Acta Neuropathologica*, 147(1), 66.
- Jankowsky, J. L., Fadale, D. J., Anderson, J., Xu, G. M., Gonzales, V., Jenkins, N. A., Copeland, N. G., Lee, M. K., Younkin, L. H., Wagner, S. L., Younkin, S. G., & Borchelt, D. R. (2004). Mutant presenilins specifically elevate the levels of the 42 residue beta-amyloid peptide in vivo: Evidence for augmentation of a 42-specific gamma secretase. *Human Molecular Genetics*, 13(2), 159–170.
- Jo, S., Yarishkin, O., Hwang, Y. J., Chun, Y. E., Park, M., Woo, D. H., Bae, J. Y., Kim, T., Lee, J., Chun, H., Park, H. J., Lee, D. Y., Hong, J., Kim, H. Y., Oh, S. J., Park, S. J., Lee, H., Yoon, B. E., Kim, Y. S., ... Lee, C. J. (2014). GABA from reactive astrocytes impairs memory in mouse models of Alzheimer's disease. *Nature Medicine*, 20(8), 886–896.
- Kabir, F., Atkinson, R., Cook, A. L., Phipps, A. J., & King, A. E. (2022). The role of altered protein acetylation in neurodegenerative disease. *Frontiers in Aging Neuroscience*, 14, 1025473.
- Khakh, B. S., & Sofroniew, M. V. (2015). Diversity of astrocyte functions and phenotypes in neural circuits. *Nature Neuroscience*, 18(7), 942–952.
- Klioueva, N. M., Rademaker, M. C., Dexter, D. T., al-Sarraj, S., Seilhean, D., Streichenberger, N., Schmitz, P., Bell, J. E., Ironside, J. W., Arzberger, T., & Huitinga, I. (2015). BrainNet Europe's code of conduct for brain banking. *Journal of Neural Transmission (Vienna)*, 122(7), 937–940.
- Klioueva, N. M., Rademaker, M. C., & Huitinga, I. (2018). Design of a European code of conduct for brain banking. *Handbook of Clinical Neurology*, 150, 51–81.
- Kumar, A., Fontana, I. C., & Nordberg, A. (2023). Reactive astrogliosis: A friend or foe in the pathogenesis of Alzheimer's disease. *Journal of Neurochemistry*, 164(3), 309–324.
- Love, S., Chalmers, K., Ince, P., Esiri, M., Attems, J., Jellinger, K., Yamada, M., McCarron, M., Minett, T., Matthews, F., Greenberg, S., Mann, D., & Kehoe, P. G. (2014). Development, appraisal, validation and implementation of a consensus protocol for the assessment of cerebral amyloid angiopathy in post-mortem brain tissue. *American Journal of Neurodegenerative Disease*, 3(1), 19–32.
- Lutz, W., Lingle, W. L., McCormick, D., Greenwood, T. M., & Salisbury, J. L. (2001). Phosphorylation of centrin during the cell cycle and its role in centriole separation preceding centrosome duplication. *The Journal of Biological Chemistry*, 276(23), 20774–20780.
- Michetti, F., D'Ambrosi, N., Toesca, A., Puglisi, M. A., Serrano, A., Marchese, E., Corvino, V., & Geloso, M. C. (2019). The S100B story: From biomarker to active factor in neural injury. *Journal of Neurochemistry*, 148(2), 168–187.
- Mirra, S. S., Heyman, A., McKeel, D., Sumi, S. M., Crain, B. J., Brownlee, L. M., Vogel, F. S., Hughes, J. P., Belle, G., Berg, L., & participating CERAD neuropathologists. (1991). The consortium to establish a registry for Alzheimer's disease (CERAD). Part II. Standardization of the neuropathologic assessment of Alzheimer's disease. *Neurology*, 41(4), 479–486.
- Montine, T. J., Phelps, C. H., Beach, T. G., Bigio, E. H., Cairns, N. J., Dickson, D. W., Duyckaerts, C., Frosch, M. P., Masliah, E., Mirra, S. S., Nelson, P. T., Schneider, J. A., Thal, D. R., Trojanowski, J. Q., Vinters, H. V., Hyman, B. T., National Institute on Aging, & Alzheimer's Association. (2012). National Institute on Aging-Alzheimer's Association guidelines for the neuropathologic assessment of Alzheimer's disease: A practical approach. *Acta Neuropathologica*, 123(1), 1–11.
- Moreno-Rodriguez, M., Perez, S. E., Nadeem, M., Malek-Ahmadi, M., & Mufson, E. J. (2020). Frontal cortex chitinase and pentraxin neuroinflammatory alterations during the progression of Alzheimer's disease. *Journal of Neuroinflammation*, 17(1), 58.
- Mrak, R. E., & Griffin, W. S. (2005). Glia and their cytokines in progression of neurodegeneration. *Neurobiology of Aging*, 26(3), 349–354.
- Mrak, R. E., & Griffin, W. S. (2001). The role of activated astrocytes and of the neurotrophic cytokine S100B in the pathogenesis of Alzheimer's disease. *Neurobiology of Aging*, 22(6), 915–922.
- Mrak, R. E., Sheng, J. G., & Griffin, W. S. (1996). Correlation of astrocytic S100 beta expression with dystrophic neurites in amyloid plaques of Alzheimer's disease. *Journal of Neuropathology and Experimental Neurology*, 55(3), 273–279.
- Nelson, P. T., Dickson, D. W., Trojanowski, J. Q., Jack, C. R., Boyle, P. A., Arfanakis, K., Rademakers, R., Alafuzoff, I., Attems, J., Brayne, C., Coyle-Gilchrist, I. T. S., Chui, H. C., Fardo, D. W., Flanagan, M. E., Halliday, G., Hokkanen, S. R. K., Hunter, S., Jicha, G. A., Katsumata, Y., ... Schneider, J. A. (2019). Limbic-predominant age-related TDP-43 encephalopathy (LATE): Consensus working group report. *Brain*, 142(6), 1503–1527.
- Oddo, S., Caccamo, A., Shepherd, J. D., Murphy, M. P., Golde, T. E., Kaye, R., Metherate, R., Mattson, M. P., Akbari, Y., & LaFerla, F. M. (2003). Triple-transgenic model of Alzheimer's disease with plaques and tangles: Intracellular Abeta and synaptic dysfunction. *Neuron*, 39(3), 409–421.
- Ogata, K., & Kosaka, T. (2002). Structural and quantitative analysis of astrocytes in the mouse hippocampus. *Neuroscience*, 113(1), 221–233.
- Perez-Nievas, B. G., & Serrano-Pozo, A. (2018). Deciphering the astrocyte reaction in Alzheimer's disease. *Frontiers in Aging Neuroscience*, 10, 114.
- Poloni, T. E., Medici, V., Carlos, A. F., Davin, A., Ceretti, A., Mangieri, M., Cassini, P., Vaccaro, R., Zaccaria, D., Abbondanza, S., Bordoni, M., Fantini, V., Fogato, E., Cereda, C., Ceroni, M., & Guaita, A. (2020). Abbiategrosso brain bank protocol for collecting, processing and characterizing aging brains. *Journal of Visualized Experiments*, 160.
- Querfurth, H. W., & LaFerla, F. M. (2010). Alzheimer's disease. *The New England Journal of Medicine*, 362(4), 329–344.
- Querol-Vilaseca, M., Colom-Cadena, M., Pegueroles, J., San Martín-Paniello, C., Clarimon, J., Belbin, O., Fortea, J., & Lleó, A. (2016). Calcium signalling toolkits in astrocytes and spatio-temporal progression of Alzheimer's disease. *Current Alzheimer Research*, 13(4), 359–369.
- Querol-Vilaseca, M., Colom-Cadena, M., Pegueroles, J., San Martín-Paniello, C., Clarimon, J., Belbin, O., Fortea, J., & Lleó, A. (2017). YKL-40 (chitinase 3-like I) is expressed in a subset of



- astrocytes in Alzheimer's disease and other tauopathies. *Journal of Neuroinflammation*, 14(1), 118.
- Reichenbach, N., Delekate, A., Plescher, M., Schmitt, F., Krauss, S., Blank, N., Halle, A., & Petzold, G. C. (2019). Inhibition of Stat3-mediated astrogliosis ameliorates pathology in an Alzheimer's disease model. *EMBO Molecular Medicine*, 11(2), e9665.
- Ren, Z., Yang, M., Guan, Z., & Yu, W. (2019). Astrocytic alpha7 nicotinic receptor activation inhibits amyloid-beta aggregation by upregulating endogenous alphaB-crystallin through the PI3K/Akt signaling pathway. *Current Alzheimer Research*, 16(1), 39–48.
- Saito, T., Matsuba, Y., Mihira, N., Takano, J., Nilsson, P., Itoharu, S., Iwata, N., & Saido, T. C. (2014). Single app knock-in mouse models of Alzheimer's disease. *Nature Neuroscience*, 17(5), 661–663.
- Serrano-Pozo, A., Gomez-Isla, T., Growdon, J. H., Frosch, M. P., & Hyman, B. T. (2013). A phenotypic change but not proliferation underlies glial responses in Alzheimer disease. *The American Journal of Pathology*, 182(6), 2332–2344.
- Serrano-Pozo, A., Mielke, M. L., Gomez-Isla, T., Betensky, R. A., Growdon, J. H., Frosch, M. P., & Hyman, B. T. (2011). Reactive glia not only associates with plaques but also parallels tangles in Alzheimer's disease. *The American Journal of Pathology*, 179(3), 1373–1384.
- Serrano-Pozo, A., Muzikansky, A., Gomez-Isla, T., Growdon, J. H., Betensky, R. A., Frosch, M. P., & Hyman, B. T. (2013). Differential relationships of reactive astrocytes and microglia to fibrillar amyloid deposits in Alzheimer disease. *Journal of Neuropathology and Experimental Neurology*, 72(6), 462–471.
- Simpson, J. E., Ince, P. G., Shaw, P. J., Heath, P. R., Raman, R., Garwood, C. J., Gelsthorpe, C., Baxter, L., Forster, G., Matthews, F. E., Brayne, C., Wharton, S. B., & MRC Cognitive Function and Ageing Neuropathology Study Group. (2011). Microarray analysis of the astrocyte transcriptome in the aging brain: Relationship to Alzheimer's pathology and APOE genotype. *Neurobiology of Aging*, 32(10), 1795–1807.
- Skrobot, O. A., Attems, J., Esiri, M., Hortobagyi, T., Ironside, J. W., Kalara, R. N., King, A., Lammie, G. A., Mann, D., Neal, J., Ben-Shlomo, Y., Kehoe, P. G., & Love, S. (2016). Vascular cognitive impairment neuropathology guidelines (VCING): The contribution of cerebrovascular pathology to cognitive impairment. *Brain*, 139(11), 2957–2969.
- Thal, D. R., Rüb, U., Schultz, C., Sassin, I., Ghebremedhin, E., Del Tredici, K., Braak, E., & Braak, H. (2000). Sequence of Abeta-protein deposition in the human medial temporal lobe. *Journal of Neuropathology & Experimental Neurology*, 59(8), 733–748.
- Thal, D. R., Rub, U., Orantes, M., & Braak, H. (2002). Phases of a beta-deposition in the human brain and its relevance for the development of AD. *Neurology*, 58(12), 1791–1800.
- Thal, D. R., Rüb, U., Schultz, C., Sassin, I., Ghebremedhin, E., del Tredici, K., Braak, E., & Braak, H. (2016). Protein carbamylation is a hallmark of aging. *Proceedings of the National Academy of Sciences of the United States of America*, 113(5), 1191–1196.
- Verkhatsky, A. (2019). Astroglial calcium signaling in aging and Alzheimer's disease. *Cold Spring Harbor Perspectives in Biology*, 11(7), a035188.
- Verkhatsky, A., Augusto-Oliveira, M., Pivoriunas, A., Popov, A., Brazhe, A., & Semyanov, A. (2021). Astroglial asthenia and loss of function, rather than reactivity, contribute to the ageing of the brain. *Pflügers Archiv*, 473(5), 753–774.
- Verkhatsky, A., Rodriguez-Arellano, J. J., Parpura, V., & Zorec, R. (2017). Astroglial calcium signalling in Alzheimer's disease. *Biochemical and Biophysical Research Communications*, 483(4), 1005–1012.
- Wang, Z., Nicholls, S. J., Rodriguez, E. R., Kummu, O., Horkko, S., Barnard, J., Reynolds, W. F., Topol, E. J., DiDonato, J. A., & Hazen, S. L. (2007). Protein carbamylation links inflammation, smoking, uremia and atherogenesis. *Nature Medicine*, 13(10), 1176–1184.
- Zhang, H., Ng, K. P., Therriault, J., Kang, M. S., Pascoal, T. A., Rosa-Neto, P., Gauthier, S., & Alzheimer's Disease Neuroimaging Initiative. (2018). Cerebrospinal fluid phosphorylated tau, visinin-like protein-1, and chitinase-3-like protein 1 in mild cognitive impairment and Alzheimer's disease. *Translational Neurodegeneration*, 7, 23.
- Zhang, Y., Sloan, S. A., Clarke, L. E., Caneda, C., Plaza, C. A., Blumenthal, P. D., Vogel, H., Steinberg, G. K., Edwards, M. S. B., Li, G., Duncan, J. A., III, Cheshier, S. H., Shuer, L. M., Chang, E. F., Grant, G. A., Gephart, M. G. H., & Barres, B. A. (2016). Purification and characterization of progenitor and mature human astrocytes reveals transcriptional and functional differences with mouse. *Neuron*, 89(1), 37–53.

## SUPPORTING INFORMATION

Additional supporting information can be found online in the Supporting Information section at the end of this article.

**How to cite this article:** Degl'Innocenti, E., Poloni, T. E., Medici, V., Olimpico, F., Finamore, F., Profka, X., Bascarane, K., Morrone, C., Pastore, A., Escartin, C., McDonnell, L. A., & Dell'Anno, M. T. (2024). Astrocytic centrin-2 expression in entorhinal cortex correlates with Alzheimer's disease severity. *Glia*, 72(12), 2158–2177. <https://doi.org/10.1002/glia.24603>